

Role of Axonal Na_v1.6 Sodium Channels in Action Potential Initiation of CA1 Pyramidal Neurons

Michel Royeck,¹ Marie-Therese Horstmann,^{1,2,3} Stefan Remy,¹ Margit Reitze,¹ Yoel Yaari,⁴ and Heinz Beck¹

¹Department of Epileptology, University of Bonn Medical Center, Bonn, Germany; ²Helmholtz-Institute for Radiation and Nuclear Physics and ³Interdisciplinary Center for Complex Systems, University of Bonn, Bonn, Germany; and ⁴Department of Physiology, Hebrew University-Hadassah School of Medicine, Jerusalem, Israel

Submitted 5 March 2008; accepted in final form 10 July 2008

Royeck M, Horstmann M-T, Remy S, Reitze M, Yaari Y, Beck H. Role of axonal Na_v1.6 sodium channels in action potential initiation of CA1 pyramidal neurons. *J Neurophysiol* 100: 2361–2380, 2008. First published July 23, 2008; doi:10.1152/jn.90332.2008. In many neuron types, the axon initial segment (AIS) has the lowest threshold for action potential generation. Its active properties are determined by the targeted expression of specific voltage-gated channel subunits. We show that the Na⁺ channel Na_v1.6 displays a striking aggregation at the AIS of cortical neurons. To assess the functional role of this subunit, we used *Scn8a^{med}* mice that are deficient for Na_v1.6 subunits but still display prominent Na⁺ channel aggregation at the AIS. In CA1 pyramidal cells from *Scn8a^{med}* mice, we found a depolarizing shift in the voltage dependence of activation of the transient Na⁺ current (*I_{NaT}*), indicating that Na_v1.6 subunits activate at more negative voltages than other Na_v subunits. Additionally, persistent and resurgent Na⁺ currents were significantly reduced. Current-clamp recordings revealed a significant elevation of spike threshold in *Scn8a^{med}* mice as well as a shortening of the estimated delay between spike initiation at the AIS and its arrival at the soma. In combination with simulations using a realistic computer model of a CA1 pyramidal cell, our results imply that a hyperpolarized voltage dependence of activation of AIS Na_v1.6 channels is important both in determining spike threshold and localizing spike initiation to the AIS. In addition to altered spike initiation, *Scn8a^{med}* mice also showed a strongly reduced spike gain as expected with combined changes in persistent and resurgent currents and spike threshold. These results suggest that Na_v1.6 subunits at the AIS contribute significantly to its role as spike trigger zone and shape repetitive discharge properties of CA1 neurons.

INTRODUCTION

In CNS neurons, graded synaptic inputs are integrated and converted to all-or-none spikes at a circumscribed region of the neuron, where spike threshold is lowest. Imaging experiments and simultaneous axonal and somatic recordings in subicular (Colbert and Johnston 1996) and cortical pyramidal neurons (Meeks and Mennerick 2007; Palmer and Stuart 2006; Stuart and Sakmann 1994; Stuart et al. 1997), as well as in Purkinje cells (Khaliq and Raman 2006; Stuart and Hausser 1994), have localized this spike triggering zone to the axon. Attempts to pinpoint this region even more precisely have revealed that in cortical neurons, spikes originate at the most distal portion of the axon initial segment (Palmer and Stuart 2006). From this site, spikes propagate along the axon and also backpropagate into the somato-dendritic compartment of the neuron.

What factors cause the axon initial segment (AIS) to have the lowest spike threshold? One factor may be a relatively high

density of Na⁺ channels in this region as evidenced in different types of neurons by immunolabelings of Na⁺ channel proteins (Boiko et al. 2001, 2003; Catterall 1981; Hossain et al. 2005; Pan et al. 2006). Indeed the AIS contains a machinery to concentrate certain types of ion channels. Ankyrin G is a key player in this process as it was shown to be both necessary and sufficient to direct different types of Na⁺ channels (Garrido et al. 2003; Zhou et al. 1998) as well as K_v7 (KCNQ) K⁺ channels (Pan et al. 2006), to the AIS. Although previous electrophysiological studies using cell-attached recordings have proclaimed a uniform transient Na⁺ current (*I_{NaT}*) density at AIS and soma (Colbert and Johnston 1996; Colbert and Pan 2002), a more recent study employing also Na⁺ imaging has argued that *I_{NaT}* density is in fact higher at the AIS than in the soma (Kole et al. 2008). The specific biophysical properties of the Na⁺ channels expressed at the AIS also may play a role in localizing the spike trigger zone to this region (Colbert and Pan 2002; Naundorf et al. 2006). In particular, it was found that Na⁺ channels at the AIS of cortical neurons exhibit a voltage dependence of activation that is shifted by ~8 mV in a hyperpolarized direction compared with somatic Na⁺ channels (Colbert and Pan 2002). However, the molecular basis for this functional specialization remains unresolved.

At the AIS, Na_v1.1, Na_v1.2, and Na_v1.6 channels have been detected on the protein level (Boiko et al. 2001, 2003; Garrido et al. 2003; Hossain et al. 2005; Ogiwara et al. 2007; Van Wart and Matthews 2006; Van Wart et al. 2007). The functional role of Na_v1.6 subunits in particular have been assessed in number of investigations in mutant mice lacking Na_v1.6 channels, for instance in cerebellar and globus pallidus neurons, as well as dorsal root and trigeminal ganglion cells (Levin et al. 2006; Mercer et al. 2007; Raman et al. 1997). The results argue for a role of Na_v1.6 subunits in mediating resurgent and persistent Na⁺ currents in these cells with a resulting effect on repetitive firing behavior.

A striking biophysical peculiarity of Na_v1.6 subunits is its hyperpolarized voltage of activation compared with other Na⁺ channel isoforms. This finding has been obtained in mouse dorsal root ganglion neurons overexpressing a TTX-insensitive variant of Na_v1.6, and thus allowing assessment of the properties of these channel isoforms in isolation in a neuronal cell (Rush et al. 2005; but see Smith et al. 1998). We therefore hypothesized that a preponderance of Na_v1.6 expression at the AIS may contribute to its low spike threshold in addition to

Address for reprint requests and other correspondence: H. Beck, Dept. of Epileptology, University of Bonn, Sigmund-Freud-Str. 25, 53105 Bonn, Germany (E-mail: heinz.beck@ukb.uni-bonn.de).

The costs of publication of this article were defrayed in part by the payment of page charges. The article must therefore be hereby marked "advertisement" in accordance with 18 U.S.C. Section 1734 solely to indicate this fact.

affecting repetitive discharge behavior. We explored the role of this channel subunit in firing behavior of CA1 pyramidal neurons using mice lacking functional Na_v1.6 subunits (*Scn8a^{med}* mice) as well as with computational modeling approaches. Our results indicate a critical role for Na_v1.6 in setting the low spike threshold at the AIS of CA1 pyramidal neurons.

METHODS

Scn8a^{med} mice

Experiments were performed on mice deficient in functional Na_v1.6 α -subunits bearing the recessive muscle endplate disease (*med*) mutation in the *Scn8a* gene. This mutation causes the expression of a truncated nonfunctional form of the protein by altering mRNA splicing due to insertion of a LINE element in exon 2 (Kohrman et al. 1996). Heterozygous breeding pairs of *Scn8a^{med/wt}* mice (C3HeB/FeJ-*Scn8a^{med}/J*; Stock No. 003798) were acquired from Jackson Laboratories (Bar Harbor, ME). Wild-type (*Scn8a^{wt}*) or mutant (*Scn8a^{med}*) homozygous littermate offspring animals aged 17–21 days were used in all experiments. All animal experiments were conducted in accordance with the guidelines of the Animal Care and Use Committee of the University of Bonn. For all experiments, animals were heart-perfused with 1–3°C cold sucrose-based artificial cerebrospinal fluid (ACSF) containing (in mM) 56 NaCl, 100 sucrose, 2.5 KCl, 1.25 NaH₂PO₄, 30 NaHCO₃, 1 CaCl₂, 5 MgCl₂, 1 kynurenic acid, and 20 glucose (95% O₂-5% CO₂) under deep anesthesia with ketamine (100 mg/kg, Pfizer) and xylazine (15 mg/kg, Bayer). After perfusion mice were decapitated, the brain was quickly removed, and 300-, 400-, or 600- μ m-thick transverse hippocampal slices were cut with a vibratome (MICROM) for electrophysiological or immunohistochemical studies.

Immunohistochemistry

Freshly cut 600- μ m hippocampal slices were placed in a tissue boat, submerged under Tissue-Tec (Sakura) and carefully frozen over liquid nitrogen before being stored at –80°C. From the frozen tissue 12- μ m-thick sections were cut with a cryostat (MICROM) and mounted to either DAKO-slides (DAKO) or Superfrost-plus-slides (Menzel) on which they were allowed to rest for 15 min at 20°C. Then the slides were fixed by submerging them for 2 min into a 1:1 mixture of ethanol and acetone (Merck) and left to dry overnight at 20°C. Finally the slides were stored in a –20°C freezer until the staining experiments were conducted.

Slides were thawed for 30 min at 20°C and afterward briefly washed in PBS (Biochrom AG.). To avoid unspecific antibody binding, the slices were incubated for 2 h at 20°C in blocking solution consisting of PBS, Triton-X100 (0.1%), fetal calf serum (10%; PAA Laboratories), and normal goat serum (5%; Vector, Burlingame, CA). All primary antibodies were diluted 1:200 in blocking solution, and the binding reaction was allowed to take place at 4°C for 12–16 h. For double immunolabelings, primary antibodies were applied together. The primary antibodies used were a monoclonal mouse anti-Ankyrin G antibody directed against the spectrin binding domain of Ankyrin G (Zymed, San Francisco, CA), a polyclonal rabbit anti-Na_v1.6 directed against amino acids 1042–1061 of the rat Na_v1.6 protein (Alomone Labs), a monoclonal mouse anti-PanNa_v antibody and a polyclonal rabbit anti-Na_v antibody, both raised against amino acids 1491–1508 of the rat Na_v1.1 protein with the antigen for the polyclonal antibody containing an additional cysteine (Noda et al. 1986), a sequence identical in all mammalian Na_v α -subunits (Sigma-Aldrich). It should be noted that the polyclonal antibody also produced a robust immunolabeling of neuronal somata in the hippocampus, which was absent with the monoclonal antibody (cf. Fig. 1, *Ab* and *B*).

Labeling of AIS, however, was similar with both antibodies. Excessive unbound primary antibodies were washed away three times at 20°C for 5 min with PBS. Subsequently, slices were incubated for 2 h at 20°C in the dark with FITC- and CY3-conjugated secondary antibodies (Dianova). Secondary antibodies were also diluted 1:200 in blocking solution and applied synchronously. Finally the slides were washed again 3 times in PBS for 5 min at 20°C and furnished with cover slips using a 1:1 mixture of Vectashield-Harding and Vectashield-Harding with DAPI cover media (Vector). The slides were then stored light protected at 4°C.

Imaging and quantification was performed using a Leica (TSC NT) confocal microscope using the LCS software (Leica) for evaluation of staining intensity. Images with different dyes were acquired sequentially. The following laser lines of an argon-krypton laser and filters were used: FITC 488 nm, DD 488/568 nm double dichroic, emission band-pass 530 \pm 30 nm and CY3 568 nm, DD 488/568 nm double dichroic and emission long-pass 590 nm. All images were acquired with a PL APO 40.0, 0.75 NA. objective (Leica). For semi-quantitative analysis of immunofluorescence, care was taken to minimize variability. First immunolabelings intended for the semi-quantitative assay were always done in one batch incorporating *Scn8a^{med}* and *Scn8a^{wt}* specimens. Second, laser power was allowed to settle for \geq 2 h prior to the imaging session. All images were taken in one continuous imaging session, where apart from focal plane all laser and microscope settings remained untouched. The pinhole was set to 0.83 Airy units. Detector gain was set to \sim 60%. To determine mean Na⁺ channel density at AIS, we first defined regions of interest (ROI) corresponding to AIS based on the Ankyrin G staining. The mean staining intensity for both Ankyrin G and PanNa_v was measured. From each section values for ten AIS were determined. We calculated the intensity of PanNa_v staining as a ratio of the average intensity in the PanNa_v channel divided by the corresponding average intensity in the Ankyrin G channel.

Storage of slices and preparation of dissociated neurons

For electrophysiological experiments, freshly cut slices were first placed into a storage chamber with room temperature (20°C) sucrose-based ACSF containing (in mM) 60 NaCl, 100 sucrose, 2.5 KCl, 1.25 NaH₂PO₄, 26 NaHCO₃, 1 CaCl₂, 5 MgCl₂, 1 kynurenic acid, and 20 glucose (95% O₂-5% CO₂) and gradually warmed to 36°C during 30 min. Subsequently, slices were equilibrated in a chamber with sucrose-free ACSF containing (in mM) 125 NaCl, 3.5 KCl, 1.25 NaH₂PO₄, 26 NaHCO₃, 2 CaCl₂, 2 MgCl₂, and 15 glucose (95% O₂-5% CO₂) for \geq 30 min at 20°C. For recordings of identified CA1 neurons in the slice preparation, 300 μ m slices were used.

For preparation of dissociated neurons, 400 μ m slices were placed in 5 ml of trituration solution containing (in mM) 145 Na-methanesulfonate, 3 KCl, 10 N-2-hydroxy-ethylpiperazine-*N'*-2-ethane sulfonic acid (HEPES), 0.5 CaCl₂, 1 MgCl₂, and 15 glucose. Solution pH was adjusted to 7.4 with NaOH. Pronase (protease type XIV; 2 mg/ml; Sigma, St. Louis, MO) was added to the oxygenated buffer (100% O₂). After two incubation periods, 10 min at 35°C and followed by 10 min at 20°C, slices were washed with pronase-free buffer saline of identical composition and transferred to a Petri dish containing 5 poly-L-lysine-coated cover slips. The CA1 region was microdissected under a binocular and triturated with fire-polished glass pipettes of decreasing aperture. Cells were allowed to settle for \geq 10 min before removing cover slips and placing them into a submerged chamber mounted on the headstage of an upright microscope (Axioskop F-2, Zeiss). Cells were equilibrated for further 10 min before recording was attempted. Whole cell recordings of dissociated neurons were performed only on pyramidal-shaped neurons with a smooth surface and a three-dimensional contour. All cells recorded possessed a clearly identifiable apical dendrite and remnants of basal dendrites and the axon.

Electrophysiology

Patch pipettes with a resistance of 3–5 MΩ were pulled from borosilicate glass capillaries (1.5 mm OD, 1 mm ID; Science Products) on a Narishige PP-830 puller (Narishige, Tokyo, Japan) and filled with the appropriate intracellular (IC) solution. Voltage- and current-clamp recordings were conducted at 20 and 30°C, respectively. Data were recorded and stored by a personal computer using a data-acquisition system (Digidata 1322A) and the pClamp9.0 software (Molecular Devices). Unless otherwise indicated data were filtered at 10 kHz and digitized at 100 kHz. Passive membrane properties were quantified as follows. The input resistance was determined in voltage clamp mode according to Ohm's law from the steady-state current response to 5- or 10-mV voltage steps (200 ms) from a –85-mV holding potential and was not significantly different between the mice from both genotypes (*Scn8a^{med}* 342.52 ± 79.00 MΩ, *Scn8a^{wt}* 300.60 ± 25.28 MΩ). Cell capacitance was determined by quantifying the charge (Qc) required to fully charge the membrane. Qc was measured as the total area under the current response to the abovementioned voltage steps, minus the charge flowing across the membrane resistance. Cell capacitance was then calculated as Qc/V, where V is the size of the voltage step (*Scn8a^{med}* 111.55 ± 15.22 pF, *Scn8a^{wt}* 100.99 ± 8.23 pF; *n* = 12 and *n* = 22, respectively).

Electrophysiology

CURRENT-CLAMP RECORDINGS. Current-clamp recordings were performed in intact CA1 neurons in the slice preparation, using a Multiclamp 700B amplifier (Molecular Devices). Whole cell configuration was obtained in voltage-clamp mode before switching to current-clamp mode, where pipette capacitance and bridge balance were monitored and carefully compensated. Cells with native membrane potential more positive than –60 mV were excluded. Subsequently, the slow current-clamp circuit of the amplifier set to 5 s was used to set the initial membrane potential prior to current injection steps to defined values. The intracellular solution used was (in mM) 130 K-gluconate, 20 KCl, 10 HEPES, 0.16 ethylene glycol-bis (2-aminoethylether)-*N,N,N',N'*-tetraacetic acid (EGTA), 2 Mg-adenosine 5'-triphosphate (ATP), and 2 Na₂-ATP; pH was titrated to 7.25 with KOH; osmolality was adjusted to 295 mosM using sucrose. For bath solution, a modified ACSF was used containing (in mM) 124 NaCl, 3.5 KCl, 26 NaHCO₃, 1.6 CaCl₂, 2 MgCl₂, and 10 glucose (95% O₂-5% CO₂). Temperature for current-clamp recordings was maintained at 30 ± 1°C. The liquid junction potential determined for these solutions was –15 mV, and all values and figures were corrected accordingly.

Analysis of current-clamp recordings

The measured resting membrane potential was not different between *Scn8a^{med}* (–72.80 ± 1.25 mV) and *Scn8a^{wt}* mice (–73.98 ± 0.66 mV). Spike thresholds were determined by measuring the voltage at which the increase in slope of the voltage trace is maximal. This time point corresponds to the maximum of the second derivation of the voltage step (d^2V/dt^2) and was determined as the time at which the third derivation of the voltage trace became zero. Spike amplitude was measured as the difference between resting membrane potential and the peak of the spike. The maximal rates of rise and decay were determined as the peak and antipeak of the second derivation of the voltage trace. Spikes during prolonged (600 ms) current injections vary systematically, depending on the time of occurrence during the current injection and the number of prior spikes. We analyzed the first, second and subsequent spikes in an action potential train separately. Analysis of these spike parameters for spikes elicited by 4-ms current injection was done using Clampfit 9.0. Repetitive firing was analyzed using an automated Igor routine that detected spikes and measured their properties.

In addition to these parameters, we determined the axo-somatic delay by assessing the delay between the two peaks observed in the second derivation of the voltage-trace. This assessment was carried out with an automated IGOR detection routine. Each automatically analyzed spike was subsequently inspected. In some cases, the automated IGOR detection routine failed to detect two peaks because of overlap between the two peaks. In these cases, an estimate of the axo-somatic delay had to be obtained by a manual determination.

The size of the spike afterdepolarization (ADP) was determined by measuring the area under the ADP starting from the beginning of the fast afterhyperpolarization to the time when membrane voltage returned to the holding potential. This delivers a value that incorporates both active and passive portions of the ADP. To evaluate the magnitude of the active portion of the ADP, we first estimated the contribution of passive components by obtaining voltage responses to subthreshold current injections of identical duration. These passive voltage responses were scaled so that the peak of the passive response was superimposed to the action potential threshold. The corresponding area approximates the passive response of the neuron, and was subtracted from the total ADP area, yielding the active component of the ADP.

VOLTAGE-CLAMP RECORDINGS. Voltage-clamp recordings of transient Na⁺ current (*I_{NaT}*) were carried out in dissociated CA1 neurons to obtain a reliable voltage control and to minimize space-clamp problems. Even in dissociated neurons, the large amplitude of *I_{NaT}* necessitated a reduction of the Na⁺ gradient between bath and intracellular solutions. The following intracellular solution was used (in mM): 110 CsF, 10 HEPES-Na, 11 EGTA, 20 tetraethylammonium-Cl, 2 MgCl₂, 0.5 guanosine 5'-triphosphate-tris(hydroxyl-methyl)-aminomethane (GTP-Tris), and 5 ATP-Na₂. Osmolality was adjusted with sucrose to 295 mosM; pH to 7.25 with CsOH. The oxygenated bath consisted of (in mM) 30 Na-methanesulphonate, 120 tetraethylammonium-Cl, 10 HEPES, 1.6 CaCl₂, 2 MgCl₂, 0.2 CdCl₂, 5 4-aminopyridine (Acros Organics), and 15 glucose. The pH was adjusted to 7.4 with HCl, osmolality was adjusted to 310 mosM with sucrose, and temperature was maintained at 20 ± 1°C. The liquid junction potential between intra- and extracellular solution was +10 mV.

Recordings of the persistent Na⁺ current (*I_{NaP}*) were carried out in intact neurons in the slice preparation with intracellular solution containing (in mM) 110 CsF, 10 HEPES-Na, 11 EGTA, 2 MgCl₂, 0.5 GTP-Tris, and 2 ATP-Na₂. Osmolality was adjusted with mannitol to 295 mosM; pH was adjusted to 7.25 (CsOH). The bath solution consisted of (in mM) 100 Na-methanesulfonate, 40 tetraethylammonium-Cl, 10 HEPES, 2 CaCl₂, 3 MgCl₂, 0.2 CdCl₂, 5 4-aminopyridine, and 15 glucose. pH 7.4, NaOH; osmolality was adjusted to 305 mosM with sucrose. Liquid junction potential was +10.0 mV.

Recordings of the resurgent Na⁺ current (*I_{NaR}*) were carried out in dissociated neurons with the intracellular solution containing (in mM) 110 CsF, 10 HEPES-Na, 11 EGTA, 2 MgCl₂, 0.5 GTP-Tris, and 2 ATP-Na₂. Osmolality was adjusted with mannitol to 295 mosM; pH was adjusted to 7.25 using CsOH. The bath solution consisted of (in mM) 100 NaCl, 40 tetraethylammonium-Cl, 10 HEPES, 2 CaCl₂, 3 MgCl₂, 0.2 CdCl₂, 5 4-aminopyridine (Acros Organics), and 15 glucose (pH 7.4, NaOH; osmolality was adjusted to 305 mosM with sucrose). Liquid junction potential was –9.99 mV.

Recordings of T-type Ca²⁺ currents (*I_{CaT}*) was carried out in slices that had been preincubated for 1 h in 5 ml oxygenated bath containing: omega-CgTx GVIA (2 μM), omega-CgTx MVIIC (3 μM), omega-AgaTx IVA (0.2 μM; Biotrend), and cytochrome C (2 mg/ml) to block N- and P/Q-type Ca²⁺ channels. Following transfer of the slices to the recording chamber, recordings were carried out with intracellular solution containing (in mM) 105 Cs-methanesulfonate, 25 tetraethylammonium-Cl, 10 HEPES, 5 EGTA, 2 MgCl₂, 2 CaCl₂, 25 sucrose, 4 ATP-Na₂, and 0.3 GTP-Tris; pH was adjusted to 7.2 with CsOH; osmolality with sucrose to 295 mosM. The bath solution

contained (in mM) 115 Na-methanesulfonate, 25 tetraethylammonium-Cl, 3.5 KCl, 2 MgCl₂, 2 CaCl₂, 4 4-aminopyridine, 10 HEPES, 25 glucose, 0.005 tetrodotoxin (Biotrend), and 0.01 nifedipine (pH 7.4, NaOH; osmolality was adjusted to 310 mosM with sucrose). Liquid junction potential was -5.0 mV.

Tight seal whole cell recordings were obtained with a seal resistance >1 G Ω in all recordings using an Axopatch 200B amplifier (Molecular Devices). Series resistance was 6 ± 2 M Ω . To improve voltage control, the prediction and compensation dials of the amplifier's series resistance compensation were set between 70 and 90% to achieve a maximal residual voltage error <2 mV (<0.5 mV for recordings of I_{NaP} , I_{NaR} , and I_{CaT}). All other recordings were excluded. Currents were recorded with the pClamp acquisition and analysis program, sampled at 100 kHz and filtered at 10 kHz (20 and 1 kHz for I_{NaP}). All potentials shown were corrected for liquid junction potentials. Recording temperature was 20°C for all voltage-clamp recordings. Unless otherwise indicated, all chemicals or drugs were obtained from Sigma.

Analysis of voltage-clamp recordings

The voltage dependence activation of I_{NaT} was determined using standard protocols (see Fig. 3A, *inset*). Peak currents were fitted using the following Boltzmann function

$$I_{(V)} = G_{\max} / (1 + \exp[(V_{1/2} - V)/k_m]) (V - V_{Na}) \quad (1)$$

where $I_{(V)}$ is the current amplitude, G_{\max} is the maximal Na⁺ conductance, $V_{1/2}$ is membrane potential at which $G_{(V)}$ is half of G_{\max} , V is the command potential, k_m is the slope at $V_{1/2}$, and V_{Na} is the Na⁺ reversal potential.

Peak currents were then converted to conductance $G_{(V)}$ using

$$G_{(V)} = I_{(V)} / (V - V_{Na}) \quad (2)$$

with V_{Na} being the Na⁺ reversal potential, V the command potential, and $I_{(V)}$ the current amplitude.

The voltage dependence of steady-state inactivation was determined using standard procedures with prepulses (500 ms) to various voltages, followed by a 10-ms test pulse to 0 mV (see Fig. 3C, *inset*). The peak currents were fitted using

$$I_{(V)} = I_{\max} / \{1 + \exp[(V_{1/2} - V)/k_m]\} \quad (3)$$

where I_{\max} is the maximal Na⁺ current, $V_{1/2}$ is membrane potential at which $I_{(V)}$ is half of I_{\max} and k_m is the slope at $V_{1/2}$.

To determine the voltage dependent activation of I_{NaP} , the TTX-subtracted current responses to the voltage ramp (Fig. 4A) were converted to conductance using Eq. 2 and subsequently fitted using Eq. 3 (Fig. 4C). In all cases, fitting was done using a Levenberg-Marquardt algorithm.

The magnitude of I_{NaR} was determined by analyzing the current responses to different 100-ms test pulses (-100 to -10 mV) following a 15-ms prepulse to 20 mV from a holding potential of 100 mV (Fig. 5A, *inset*). The amplitude of I_{NaR} was determined as the peak current during the test pulse minus the steady-state current at the end of the test pulse (see Fig. 5A).

The amplitude of I_{CaT} was determined by fitting the tail current following a 20-ms depolarization with a biexponential function (see Fig. 6A, *inset*) using a Levenberg-Marquardt algorithm. Under our recording conditions, the faster deactivating current component represents R-type Ca²⁺ currents, while the slower component is due to deactivation of T-type Ca²⁺ currents (Sochivko et al. 2002). The amplitude corresponding to the slower deactivating component was derived by extrapolation of the fitted curve to the end of the depolarizing voltage step.

All data are presented as averages \pm SE. For comparison of means, a two-tailed Student's *t*-test was performed as appropriate. Differ-

ences between axo-somatic spike delay and input-output relations between *Scn8a^{med}* and *Scn8a^{wt}* mice, were analyzed by MANOVA. For all tests, the significance level was set at $P < 0.05$. All data analyses were done with the Clampfit 9.0 software (Molecular Devices), Origin 7 (OriginLab, Northampton, MA), IGOR (Wavemetrics, Lake Oswego, OR), SPSS 14.0 (SPSS) and Excel 2003 at a Windows based PC-system (Microsoft, Redmond, WA).

Modeling of a CA1 pyramidal neuron

We have created a model of a CA1 neuron with a realistic morphology and different voltage- and Ca²⁺-dependent currents with differential subcellular distribution. The modeling environment was Microsoft Windows XP, running on a dual core processor, each Intel Processor with 2.39 GHz, 1.97 GB Ram. The simulation was implemented within the simulation software NEURON (Carnevale and Hines 2006). The integration time steps were fixed at 0.01 ms. The general approach to model the properties of different ionic currents is based on a Hodgkin-Huxley-type formalism (Hodgkin and Huxley 1952), where the voltage and time dependence of currents flowing through ion channels is governed by gating particles that determine the opening and closing of the channel pore. The time- and place-dependent total current density $i_m(x, t)$ through a cell membrane is given by

$$i_M(x, t) = c_M(x) \frac{dE(x, t)}{dt} + \sum_j i_j(x, t)$$

where x denotes the place, t time, c_M capacitance per cm², E the membrane potential, and j denotes the distinct currents incorporated in our model.

The dynamics of gating particles is governed by the differential equation

$$\frac{dp}{dt} = \frac{p_\infty - p}{\tau_p}$$

where p denotes the fraction of gating particles being in a state that allows the channel to be open, p_∞ denotes the equilibrium state, and τ_p the time constant of the dynamics. In general p_∞ and τ_p can be dependent on the membrane voltage and ionic concentrations. The functional dependencies are given in descriptions of the individual currents. Abbreviations for variables and constants are explained in Table 1. The maximum conductances \bar{g} with which the currents occur in the different parts of the model neuron are given in Table 2. The current through an ion channel is then given by Ohm's law. For the

TABLE 1. Table of constants and variables used in the modelling section

Symbol	Meaning
i , A/m ²	Current density
E , mV	Membrane potential
g , mS/cm ²	Conductance
T [K] or [°C]	Temperature
c , F/cm ²	Capacitance per area
x , cm	Place
t , ms	Time
j	Index variable
p	Gating particle
α, β , ms ⁻¹	Transition rates
$F = 96520$, C/M	Faraday constant
$R = 8.3134$, J/(M°C)	Gas constant
$[Ca^{2+}]_i$ or $[Ca^{2+}]_o$, mM	Intracellular or extracellular cell Ca ²⁺ concentration
x	Place
P , cm/s	Permeability

TABLE 2. Maximal conductances g of the currents included in the model

Name of Current	Soma, mS/cm ²	Dendrites, mS/cm ²	Distal Apical Dendrites, mS/cm ²	Axon, mS/cm ²	AIS, mS/cm ²
i_{NaT}	100	5.2085	5.2085	80	20 to 1000
i_{NaP}	1	—	—	—	0.5
i_{NaT-In}	0.75	—	—	—	0.5
i_{KDR}	5	0.5	0.5	25	20
i_{KA}	5	40	60	20	20
i_{KM}	2	—	—	4	4
i_{KCT}	10	—	—	—	—
i_{AHP}	0.7	—	—	—	—
i_{CaT}	1.1×10^{-5}	—	1.1×10^{-5}	—	—
i_{CaL}	6.622×10^{-5}	—	—	—	—
i_{CaR}	4.4×10^{-5}	—	—	—	—
i_{Campq}	1.54×10^{-4}	—	—	—	—
i_H	0.05	0.3	1.1×10^{-5}	—	—

Ca²⁺ currents Ohm's law was replaced by the Goldman-Hodgkin-Katz-equation.

Neuronal morphology

The morphology of the CA1 model neuron is adapted from Varona et al. (2000) and comprises 265 sections (829 segments) with branched basal and apical dendrite, soma, and an axon. It is based on a detailed morphometric study of average compartment dimensions, branching pattern, and tapering (Bannister and Larkman 1995).

Passive electrophysiological properties

Passive parameters were also adapted from Varona et al. (2000) and include values for the specific membrane capacitance, the membrane resistivity, and the resistivity of the cytoplasm. Leak currents were assumed to have a reversal potential of -70 mV.

Temperature dependence

The dependence of ion channel dynamics on the environmental temperature T can be expressed by $Q(T) = Q_{10}^{(T-T_0)/10K}$ varies for different ion channels and can be different for activation ($Q_{10,activation}$), inactivation ($Q_{10,inactivation}$), and current amplitude ($Q_{10,amplitude}$). The values for T_0 are given in the description of the individual currents. The dependence of the ion channel dynamics on $Q(T)$ was applied according to published data (see citations in the description of the individual currents). Simulations were performed for a temperature $T = 30^\circ\text{C}$.

Na⁺ currents

The equilibrium potential for Na⁺ was $E_{Na} = 55$ mV.

Transient Na⁺ current

The somatic i_{NaT} was modeled according to Migliore et al. (1999)

$$i_{NaT} = \bar{g}_{Na} \cdot m^3 \cdot h \cdot s \cdot (E - E_{Na})$$

with m , h , and s corresponding to the gating parameter for fast activation, fast inactivation, and slow-inactivation, respectively.

The equations describing activation were as follows

$$\alpha_m = \frac{0.4 \text{ ms}^{-1} \cdot (E + 30 \text{ mV} - \Delta V_{1/2})}{1 - \exp[-(E + 30 \text{ mV} - \Delta V_{1/2})/7.2 \text{ mV}]}$$

$$\beta_m = \frac{0.124 \text{ ms}^{-1} \cdot (E + 30 \text{ mV} - \Delta V_{1/2})}{1 - \exp[(E + 30 \text{ mV} - \Delta V_{1/2})/7.2 \text{ mV}]}$$

$$\tau_m = \frac{1}{Q(T) \cdot (\alpha_m + \beta_m)}$$

if $\tau_m < 0.02$ ms then $\tau_m = 0.02$ ms

$$m_\infty = \frac{\alpha_m}{\alpha_m + \beta_m}$$

The parameter $\Delta V_{1/2}$ was used to introduce a shift in the midpoint of the activation curve. This parameter was zero for the somatic i_{NaT} . The equations describing fast inactivation were as follows

$$\alpha_h = \frac{0.03 \text{ ms}^{-1} \cdot (E + 45)}{1 - \exp[-(E + 45)/1.5 \text{ mV}]}$$

$$\beta_h = \frac{-0.01 \text{ ms}^{-1} - (E + 45 \text{ mV})}{1 - \exp[(E + 45 \text{ mV})/1.5 \text{ mV}]}$$

$$\tau_h = \frac{1}{Q(T) \cdot (\alpha_h + \beta_h)}, \quad \text{if } \tau_h < 0.5 \text{ ms then } \tau_h = 0.5 \text{ ms}$$

$$h_\infty = \frac{1}{1 + \exp[(E + 50 \text{ mV})/4 \text{ mV}]}$$

The equations describing slow inactivation were as follows

$$\alpha_s = 1 \text{ ms}^{-1} \cdot \exp\left(\frac{139.24 \text{ mV}^{-1} \cdot (E + 60 \text{ mV})}{T[K]}\right)$$

$$\beta_s = 1 \text{ ms}^{-1} \cdot \exp\left(\frac{27.85 \text{ mV}^{-1} \cdot (E + 60 \text{ mV})}{T[K]}\right)$$

$$s_\infty = 1$$

$$\tau_s = \frac{\beta_s}{0.0003 \cdot (1 + \alpha_s)}, \quad \text{if } \tau_s < 10 \text{ ms then } \tau_s = 10 \text{ ms}$$

We assumed $T_0 = 24^\circ\text{C}$, the Q_{10} values were derived from Migliore et al. (1999).

The Na⁺ current at the AIS was identical to the somatic Na⁺ current but lacked the slow inactivation process. The parameter $\Delta V_{1/2}$, which produces a shift of the activation behavior, was systematically varied as described in RESULTS.

Persistent Na⁺ current

The persistent Na⁺ current (i_{NaP}) is a fast activating and noninactivating current

$$i_{\text{NaP}} = \bar{g}_{\text{NaP}} \cdot m \cdot (E - E_{\text{Na}})$$

The dynamics of the activating gating particle m are

$$m_{\infty} = \frac{1}{1 + \exp[-(E + 52.3 \text{ mV})/6.8 \text{ mV}]}$$

$$\tau_m = 1 \text{ ms}$$

$i_{\text{NaT-In}}$ corresponds to a Na^+ current with intermediate inactivation kinetics, which is observed in CA1 neurons (Yue et al. 2005)

$$i_{\text{NaT-In}} = \bar{g}_{\text{NaT-In}} \cdot m \cdot h$$

The dynamics of the activation gate particle are

$$m_{\infty} = \frac{1}{1 + \exp[-(E + 52.6)/4.6]}$$

$$\tau_m = 1 \text{ ms}$$

The inactivation dynamics were derived from Magistretti and Alonso (1999)

$$\alpha_h = \frac{(2.88 \cdot E - 49 \text{ mV}) \text{ mV}^{-1} \text{ ms}^{-1}}{1 - \exp[(E + 17.01 \text{ mV})/4.63 \text{ mV}]}$$

$$\beta_h = \frac{(6.94 \cdot E + 447 \text{ mV}) \text{ mV}^{-1} \text{ ms}^{-1}}{1 - \exp[-(E + 64.41 \text{ mV})/2.63 \text{ mV}]}$$

$$\tau_h = \frac{1}{(\alpha_h + \beta_h)}$$

$$h_{\infty} = \frac{\alpha_h}{\alpha_h + \beta_h}$$

K^+ currents

The equilibrium potential for K^+ was $E_K = -95 \text{ mV}$.

Delayed rectifier K^+ current

The delayed rectifier K^+ current (i_{KDR}) was modeled according to Golomb et al. (2006)

$$i_{\text{KDR}} = \bar{g}_{\text{KDR}} \cdot n^4 \cdot (E - E_K)$$

with the following activation dynamics

$$n_{\infty} = \frac{1}{1 + \exp[-(E + 35 \text{ mV})/10 \text{ mV}]}$$

$$\tau_n = 0.1 \text{ ms} + \frac{0.5 \text{ ms}}{1 + \exp[(E + 27 \text{ mV})/15 \text{ mV}]}$$

A-type K^+ current

The A-type K^+ current (i_{KA}) was modeled according to Golomb et al. (2006)

$$i_{\text{KA}} = \bar{g}_{\text{KA}} \cdot a^3 \cdot b \cdot (E - E_K)$$

The activation dynamics were as follows

$$a_{\infty} = \frac{1}{1 + \exp[-(E + 50 \text{ mV})/20 \text{ mV}]}$$

$$\tau_a = 0.5 \text{ ms}$$

The inactivation dynamics were as follows

$$b_{\infty} = \frac{1}{1 + \exp[(E + 80 \text{ mV})/6 \text{ mV}]}$$

$$\tau_b = 15 \text{ ms}$$

M-type K^+ current

The M current (i_{KM}) was modeled according to Warman et al. (1994)

$$i_{\text{KM}} = \bar{g}_{\text{KM}} \cdot u^2 \cdot (E - E_K)$$

We assumed $T_0 = 23^\circ\text{C}$. Q_{10} values for i_{KM} were derived from Halliwell and Adams (1982).

Activation dynamics

$$\alpha = \frac{0.016 \text{ ms}^{-1}}{\exp[-(E + 52.7 \text{ mV})/23 \text{ mV}]}$$

$$\beta = \frac{0.016 \text{ ms}^{-1}}{\exp[(E + 52.7 \text{ mV})/18.8 \text{ mV}]}$$

$$u_{\infty} = \frac{\alpha}{\alpha + \beta}$$

$$\tau_u = \frac{3}{Q(T) \cdot (\alpha + \beta)}$$

Voltage- and Ca^{2+} -dependent K^+ current

This K^+ current (i_{KCT}) adapted from Stacey and Durand (2000) is dependent both on the intracellular Ca^{2+} concentration $[\text{Ca}]_{\text{i},1}$ and on the membrane potential E . For the dynamics of the Ca^{2+} ions see following text

$$i_{\text{KCT}} = \bar{g}_{\text{KCT}} \cdot c^2 \cdot d \cdot (E - E_K)$$

The Ca^{2+} dependence was implemented as follows

$$\nu_{\text{shift}} = -40 \cdot \log_{10}([\text{Ca}^{2+}]_{\text{i},1}) \quad \text{where} \quad [\text{Ca}^{2+}]_{\text{i},1} \text{ is given in [mM].}$$

$$\alpha = 0.0077 \text{ ms}^{-1} \text{ mV}^{-1} \cdot \frac{E + \nu_{\text{shift}} + 103 \text{ mV}}{1 - \exp[-(E + \nu_{\text{shift}} + 103 \text{ mV})/12 \text{ mV}]}$$

$$\beta = \frac{1.7 \text{ ms}^{-1}}{\exp[(E + \nu_{\text{shift}} + 237 \text{ mV})/30 \text{ mV}]}$$

$$c_{\infty} = \frac{\alpha}{\alpha + \beta}$$

$$\tau_c = 0.55 \text{ ms}$$

The voltage dependence of gating was defined as follows

$$\alpha = \frac{1 \text{ ms}^{-1}}{\exp[(E + 79 \text{ mV})/10 \text{ mV}]}$$

$$\beta = \frac{4 \text{ ms}^{-1}}{1 + \exp[-(E - 82 \text{ mV})/27 \text{ mV}]}$$

$$d_{\infty} = \frac{\alpha}{\alpha + \beta}$$

$$\tau_d = \frac{1}{\alpha + \beta}$$

Ca²⁺-dependent K⁺ current

The gating properties of this K⁺ current (i_{KAHP}) are only dependent on the intracellular Ca²⁺ concentration $[\text{Ca}^{2+}]_{\text{i},2}$ and is therefore in our model restricted to the somatic compartment

$$i_{\text{KAHP}} = \bar{g}_{\text{KAHP}} \cdot q \cdot (E - E_K)$$

Activation dynamics

$$\alpha = \frac{0.0048 \text{ ms}^{-1}}{\exp\{-[10 * \log_{10}([\text{Ca}^{2+}]_{\text{i},2}) - 35]/2\}}$$

$$\beta = \frac{0.012 \text{ ms}^{-1}}{\exp\{[10 * \log_{10}([\text{Ca}^{2+}]_{\text{i},2}) \div 100]/5\}}$$

In both rate functions, $[\text{Ca}^{2+}]_{\text{i},2}$ is given in mM

$$q_{\infty} = \frac{\alpha}{\alpha + \beta}$$

$$\tau_q = 48 \text{ ms}$$

These dynamics were implemented according to Stacey and Durand (2000) and Warman et al. (1994).

Ca²⁺ currents

The maximal permeabilities \bar{P} of the various Ca²⁺ channels were chosen from investigations reported in Takahashi and Akaike (1991) and Su et al. (2002).

T-type Ca²⁺ current

The T-type Ca²⁺ current (i_{CaT}) is mainly based on findings reported in Lee et al. (1999) and Klöckner et al. (1999)

$$i_{\text{CaT}} = \bar{P}_{\text{CaT}} \cdot m^2 \cdot h \cdot \frac{4F^2E}{RT} \cdot \frac{[\text{Ca}]_{\text{O}} - [\text{Ca}]_{\text{i},1} \cdot \exp(2FE/RT)}{1 - \exp(2FE/RT)}$$

For this and the other Ca²⁺ currents, $E < 10^{-4}$ mV $1/1 - \exp(E)$ was approximated by the first terms of a Taylor expansion $-1 + E/2$ because the term $\exp(2FE/RT)$ is present at the denominator of the preceding equation, and so the denominator would become 0 when $E = 0$.

Activation dynamics

$$m_{\infty} = \left(\frac{1}{1 + \exp[-(E + 31.4 \text{ mV})/8.8 \text{ mV}]} \right)^{0.5}$$

$$\tau_m = \left(\frac{1 \text{ ms}}{1 + \exp[-(E - 7.63 \text{ mV})/28.47 \text{ mV}]} \right) + 0.01 \text{ ms} \cdot$$

$$\left(\frac{62.82 \text{ ms}}{1 + \exp[(E + 37.02 \text{ ms})/5.27 \text{ ms}]} + 3.78 \text{ ms} \right) \cdot \frac{1}{Q(T)}$$

Inactivation dynamics

$$h_{\infty} = \frac{1}{1 + \exp[(E + 72 \text{ mV})/3.7 \text{ mV}]}$$

$$\tau_h = \frac{1 \text{ ms} \cdot \{1 + \exp[(E + 65.77 \text{ mV})/4.32 \text{ mV}]\}}{0.0021 \cdot Q(T) \cdot \{1 + \exp[(E + 72 \text{ mV})/3.7 \text{ mV}]\}}$$

For the temperature dependence, we assumed $T_0 = 23^\circ\text{C}$. Q_{10} values for i_{CaT} were derived from Coulter et al. (1989).

R-type Ca²⁺ current

The R-type Ca²⁺ current (i_{CaR}) was modeled with current parameters taken from Sochivko et al. (2003) and Randall and Tsien (1997)

$$i_{\text{CaR}} = \bar{P}_{\text{CaR}} \cdot m \cdot h \cdot \frac{4F^2E}{RT} \cdot \frac{[\text{Ca}]_{\text{O}} - [\text{Ca}]_{\text{i},1} \cdot \exp(2FE/RT)}{1 - \exp(2FE/RT)}$$

Activation dynamics

$$m_{\infty} = \frac{1}{1 + \exp(-(E + 15 \text{ mV})/5.8 \text{ mV})}$$

$$f_1(E) = \frac{1}{1 + \exp[-(E + 15.2 \text{ mV})/4.29 \text{ mV}]} + 0.0222$$

$$f_2(E) = \frac{15.244}{1 + \exp[(E + 13.44 \text{ mV})/8.61 \text{ mV}]} + 0.511$$

$$\tau_m = \frac{1 \text{ ms} \cdot f_1(E) \cdot f_2(E)}{Q(T)}$$

Inactivation dynamics

$$h_{\infty} = \frac{1}{1 + \exp[(E + 78.7 \text{ mV})/14.5 \text{ mV}]}$$

$$f_1(E) = \frac{1}{1 + \exp[-(E + 49.8 \text{ mV})/2.64 \text{ mV}]}$$

$$f_2(E) = \frac{45.11}{1 + \exp(E/8.92 \text{ mV})}$$

$$\tau_h = \frac{f_1(E) \cdot f_2(E) \cdot 1 \text{ ms} + 22.7 \text{ ms}}{Q(T)}$$

For the temperature dependence, we assumed T_0 . Q_{10} values were derived from McAllister-Williams and Kelly (1995).

L-type Ca²⁺ current

The L-type Ca²⁺ current (i_{CaL}) was modeled as follows:

Activation dynamics

$$i_{\text{CaL}} = Q(T) \cdot \bar{P}_{\text{CaL}} \cdot m^2 \cdot \frac{2 \cdot 10^{-5} \text{ mM}}{2 \cdot 10^{-5} \text{ mM} + [\text{Ca}^{2+}]_{\text{i},1}}$$

$$\frac{4F^2E}{RT} \cdot \frac{[\text{Ca}^{2+}]_{\text{O}} - [\text{Ca}^{2+}]_{\text{i},1} \cdot \exp(2FE/RT)}{1 - \exp(2FE/RT)}$$

$$m_{\infty} = \left(\frac{1}{1 + \exp[-(E + 11 \text{ mV})/5.7 \text{ mV}]} \right)^{0.5}$$

$$\alpha_m = 0.1967 \text{ mV}^{-1} \cdot \frac{E - 34.88 \text{ mV}}{1 - \exp\{-(E - 34.88 \text{ mV})/10 \text{ mV}\}}$$

$$\beta_m = 0.046 \cdot \exp[-(E - 15 \text{ mV})/20.73 \text{ mV}]$$

$$\tau_m = \frac{1}{Q(T)(\alpha_m + \beta_m)}$$

For the temperature dependence, we assumed $T_0 = 21^\circ\text{C}$. X_{10} values were derived from McAllister-Williams and Kelly (1995).

N- and P/Q-type Ca^{2+} current

The high-threshold Ca^{2+} currents (i_{Canpq}) mediated by the N- and P/Q-type were summarized into a single current with the following properties

$$i_{\text{Canpq}} = \bar{P}_{\text{Canpq}} \cdot Q(T) \cdot m^2 \cdot \frac{4F^2E}{RT} \cdot \frac{[\text{Ca}]_o - [\text{Ca}]_{i,i} \cdot \exp(2FE/RT)}{1 - \exp(2FE/RT)}$$

Activation dynamics

$$m_\infty = \left(\frac{1}{1 + \exp[-(E + 11 \text{ mV})/5.7 \text{ mV}]} \right)^{0.5}$$

$$\alpha = \frac{0.1967 \text{ ms}^{-1} \cdot [(E - 15 \text{ mV}) + 19.88 \text{ mV}]}{1 - \exp\{[(E - 15 \text{ mV}) + 19.88 \text{ mV}]/10.0 \text{ mV}\}}$$

$$\beta = 0.046 \text{ ms}^{-1} \cdot \exp[-(E - 15 \text{ mV})/20.73 \text{ mV}]$$

$$\tau_m = \frac{1}{Q(T) - (\alpha + \beta)}$$

Temperature dependence: $T_0 = 21^\circ\text{C}$ for q_{ampl} and $T_0 = 22^\circ\text{C}$ for q_m . Q_{10} values were derived from McAllister-Williams and Kelly (1995).

Ca^{2+} dynamics

As in Warman et al. (1994), the intracellular Ca^{2+} dynamics were modeled assuming two distinct intracellular Ca^{2+} pools with appropriate dynamics, given by

$$\frac{[\text{Ca}^{2+}]_{i,n}}{dt} = \frac{[\text{Ca}^{2+}]_{\infty,n} - [\text{Ca}^{2+}]_{n,i}}{\tau_{\text{Ca},n}} - f_a \cdot \frac{i_{\text{Ca}}}{2F\delta_n}$$

The particular pool is indexed by n . Apart from the diffusion contribution, $[\text{Ca}^{2+}]_{n,i}$ is changed due to the total Ca^{2+} current density i_{Ca} , which is the sum of i_{Canpq} , i_{CaR} , i_{CaL} , and i_{CaT} . $[\text{Ca}^{2+}]_{\infty,n}$ denotes the intracellular Ca^{2+} concentration for large times and closed Ca^{2+} channels. $\tau_{\text{Ca},n}$ is the associated time constant of diffusion. f_n denotes the fraction of the Ca^{2+} current density that is active in pool n and i_{Ca}/δ_n is the rate of Ca^{2+} removal per volume. We assume an inner shell thickness δ_n , which is filled with Ca^{2+} . The parameters of the two pools are as follows

$$[\text{Ca}]_{\infty,1} = [\text{Ca}]_{\infty,2} = 10^{-1} \text{ mM}$$

$$\tau_{\text{Ca},1} = 1 \text{ ms, in the soma}$$

$$\tau_{\text{Ca},1} = 1 \text{ ms, in the dendrites}$$

$$\tau_{\text{Ca},2} = 1000 \text{ ms}$$

$$f_1 = 1$$

$$f_2 = 0.012$$

$$\delta_1 = \delta_2 = 0.5 \text{ } \mu\text{m}$$

Pool 1 is present in the soma and in the dendrites; pool 2 is only present in the soma. The extracellular Ca^{2+} concentration was set to $[\text{Ca}]_o = 2 \text{ mM}$.

Hyperpolarization activated h -current

This unspecific cationic current i_h is activated by hyperpolarization and modeled according to Gasparini et al. (2004)

$$i_h = \bar{g}_h \cdot l \cdot (E + 30 \text{ mV})$$

Activation dynamics

$$l_\infty = \frac{1}{1 + \exp[0.1512 \text{ mV}^{-1} \cdot (E + 90 \text{ mV})]}$$

$$\tau_l = \frac{\exp(0.03326 \text{ mV}^{-1} \cdot (E + 75 \text{ mV}))}{Q(T) \cdot 0.011 \text{ ms}^{-1} \cdot \{1 + \exp[0.08316 \text{ mV}^{-1} \cdot (E + 75 \text{ mV})]\}}$$

For the temperature dependence, we assumed $T_0 = 33^\circ\text{C}$. Q_{10} values were derived from Gasparini et al. (2004).

Induction of spiking

Current injections were introduced into the soma at $t = 100 \text{ ms}$ for 4 ms. Stimulus intensity was increased in steps of 0.01 nA. For analysis, we chose the lowest stimulus amplitude to which the model neuron responded with a spike to the current injection.

RESULTS

Subcellular distribution of Na^+ channels in the CA1 region of the hippocampus

$\text{Na}_v1.6$ channels are strongly concentrated at AIS of different types of neurons in the CNS (Boiko et al. 2003; Hossain et al. 2005; Van Wart and Matthews 2006; Van Wart et al. 2007). We examined whether $\text{Na}_v1.6$ is similarly expressed in CA1 pyramidal cells using double immunolabeling for Ankyrin G (a marker for AIS) (see for instance Garrido et al. 2003) and for $\text{Na}_v1.6$ in hippocampal sections. In the CA1 region, $\text{Na}_v1.6$ subunits were clearly aggregated at the AIS (Fig. 1Aa, see insets for larger magnification of individual AIS, stratum pyramidale, oriens, and alveus indicated by SP, SO, and AL, respectively). Additionally, double immunolabeling with a Pan Na_v antibody and the $\text{Na}_v1.6$ antibody revealed a concentration of both immunolabels at AIS (Fig. 1Ab). Mice lacking functional $\text{Na}_v1.6$ channels due to a truncation mutation in exon 2 of the *Scn8a* gene (*Scn8a^{med}*) were devoid of $\text{Na}_v1.6$ immunoreactivity, but Pan Na_v immunoreactive AIS were still present (Fig. 1B). These experiments also revealed that $\text{Na}_v1.6$ channel aggregation at AIS constitutes a general feature of cortical neurons as it was also found in dentate granule and CA3 pyramidal cells, and in subicular and neocortical neurons (Fig. 1C).

In *Scn8a^{med}* mice, AIS were present in undiminished numbers and did not appear altered in immunolabelings for Ankyrin G (Fig. 2A, compare leftmost micrographs). Moreover, immunolabeling with the Pan Na_v antibody produced a robust signal at AIS of *Scn8a^{med}* mice (Fig. 2A, compare rightmost micrographs, see also Fig. 1, Ab and B). We therefore analyzed the density of Na^+ channel proteins at *Scn8a^{wt}* and *Scn8a^{med}* mice AIS in a semi-quantitative manner. Double immunolabelings for Ankyrin G and Pan Na_v allowed us to

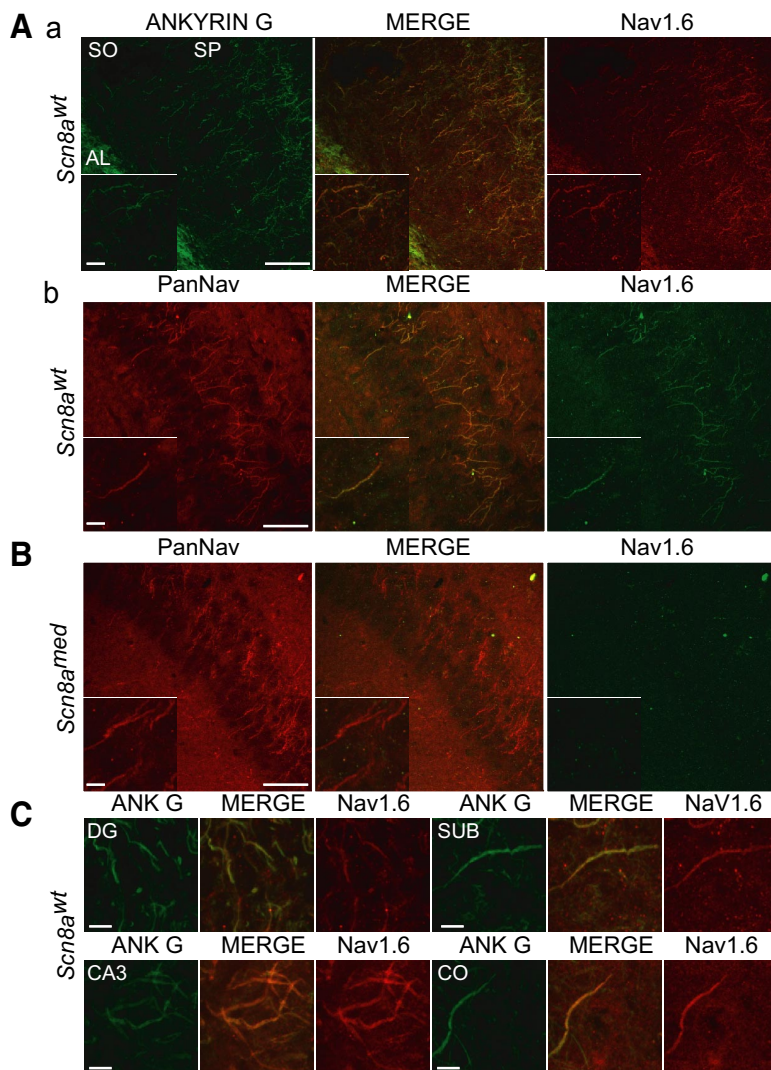


FIG. 1. Axon initial segment localization of Na⁺ channels in central neurons of *Scn8a^{med}* and *Scn8a^{wt}* mice. *A,a*: in *Scn8a^{wt}* animals, a monoclonal Ankyrin G antibody, a marker for axon initial segment (AIS, green, *leftmost panel*), colocalizes with a polyclonal antibody directed against Na_v1.6 (red, *rightmost panel*, merged in the *middle panel*). *Insets* (*bottom left*) in this and *B* and *C* correspond to higher magnifications of individual AIS. SP, stratum pyramidale; SO, stratum oriens; AL, alveus. *B*: Na_v1.6 also colocalizes with the immunolabeling obtained with a monoclonal PanNa_v antibody. *B*: staining pattern for Na_v1.6 and PanNa_v in *Scn8a^{med}* mice. No detectable staining is observed for Na_v1.6, whereas the PanNa_v antibody yields a pronounced staining of AIS. *C*: AIS staining with Na_v1.6 antibodies (red) and Ankyrin G (green) in different types of neurons as indicated: DG, dentate gyrus; SUB, subiculum; CO, cortex. Scale bars correspond to 50 μ m in main panels and 5 μ m in the *insets*.

demarcate individual AIS in the Ankyrin G channel (Fig. 2*A*, *leftmost panels*, see *insets* for larger magnification) and to determine the intensity of the PanNa_v immunolabeling within this region of interest (see METHODS, *Scn8a^{wt}*: 8 slices from 5 mice, *Scn8a^{med}*: 10 slices from 5 mice; 10 AIS were analyzed in each slice). Indeed the ratios of PanNa_v to Ankyrin G immunolabeling intensities at *Scn8a^{wt}* and *Scn8a^{med}* mice AIS were the same (1.5 ± 0.1 and 1.3 ± 0.04 , respectively, $P > 0.05$; Fig. 2*B*). The lack of a significant reduction in PanNa_v staining at AIS of *Scn8a^{med}* mice suggests that the absence of Na_v1.6 subunits allows other Na_v subunits to accumulate at the AIS. This is in good agreement with Van Wart and Mathews. (2006) and supported by the finding that Na_v1.6 channels share with Na_v1.1 and Na_v1.2 channels Ankyrin G binding motifs that confer targeting to the axon (Garrido et al. 2003; Pan et al. 2006).

Absence of Na_v1.6 positively shifts I_{NaT} activation

It has been previously hypothesized that I_{NaT} at the AIS activates at more negative voltages than I_{NaT} at the soma, causing spikes to commence at or close to the AIS (Colbert and Pan 2002). This peculiarity may be due to selective accumu-

lation of Na_v1.6 channels at the AIS because these channels were shown to activate at more negative voltages than other Na⁺ channels when expressed in cultured dorsal root ganglion neurons (Rush et al. 2005). If this is the case, loss of Na_v1.6 channels in native CA1 neurons should lead to a depolarizing shift in I_{NaT} activation curve. To test this, we performed whole cell recordings of I_{NaT} in dissociated CA1 pyramidal neurons of *Scn8a^{wt}* and *Scn8a^{med}* mice ($n = 6$ and $n = 7$, respectively). A representative family of I_{NaT} traces evoked by increasing voltage steps in *Scn8a^{wt}* (*topmost traces*) and *Scn8a^{med}* (*bottom traces*) neurons are shown in Fig. 3*A* (voltage protocols shown in the *inset*). From this data, we constructed the I_{NaT} activation curve for each of the tested neurons by fitting it with a Boltzmann function (see METHODS). The peak conductance of I_{NaT} was not significantly different between the groups of neurons (*Scn8a^{wt}*: 69.2 ± 10.5 nS, $n = 8$; *Scn8a^{med}*: 59.8 ± 6.5 nS, $P > 0.05$, $n = 11$). The averaged normalized data for each group of neurons are provided in Fig. 3*B*. We found that the I_{NaT} activation curve was ~ 5 mV more positive in mutant neurons ($V_{1/2} = -25.00 \pm 1.18$ mV) than in wild-type neurons ($V_{1/2} = -29.77 \pm 1.00$ mV, $P = 0.008$; Fig. 3*B*). The steepness of the activation curve was not significantly different between the two groups (slope factor $k_m = 5.87 \pm 0.48$ mV for

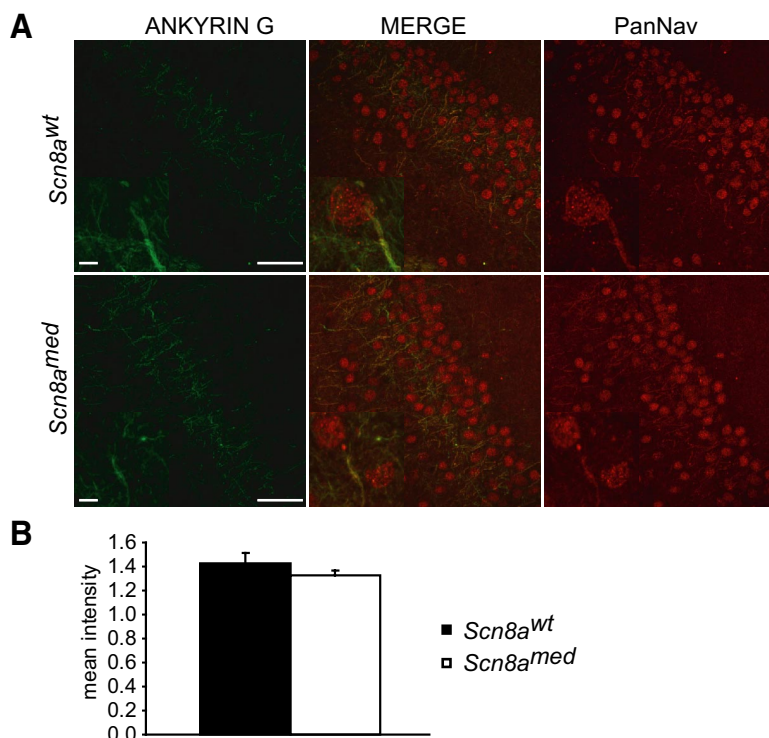


FIG. 2. Semi-quantitative analysis of fluorescence intensity of PanNav relative to Ankyrin G in slices obtained from *Scn8a^{med}* and *Scn8a^{wt}* mice. **A**: representative examples of double immunofluorescence labelings with the monoclonal Ankyrin G antibody (green) and a polyclonal PanNav antibody (red) used for quantification of PanNav staining at AIS, in *Scn8a^{wt}* mice (top) and *Scn8a^{med}* mice (bottom). **B**: average AIS fluorescence intensity of PanNav relative to Ankyrin G in *Scn8a^{wt}* mice (black bar, 10 AIS analyzed in each of 8 slices obtained from 5 animals) and *Scn8a^{med}* mice (white bar, 10 AIS analyzed in each of 10 slices obtained from 5 animals, $P > 0.05$), for a detailed description of the semi-quantitative analysis of PanNav staining at AIS see METHODS. Scale bars correspond to 50 μm in main panels and 5 μm in the insets.

Scn8a^{wt} and $k_m = 5.37 \pm 0.39$ mV for *Scn8a^{med}* neurons; $P > 0.05$).

We also compared the two groups of neurons with respect to steady-state inactivation of I_{NaT} . Representative families of I_{NaT} traces evoked by a depolarizing step to 0 mV preceded by 500-ms-long prepulses to various potentials in neurons from a *Scn8a^{wt}* (topmost) and *Scn8a^{med}* (bottom) mouse are shown in Fig. 3C (voltage protocols shown in the inset). From these data, we constructed the I_{NaT} steady-state inactivation curve for each of the tested neurons by fitting it with a Boltzmann function (see METHODS). The averaged data for each group of neurons are provided in Fig. 3D. In contrast to the marked difference in I_{NaT} activation, steady-state inactivation was similar in the two groups of neurons.

Absence of $\text{Na}_v1.6$ reduces the persistent Na^+ current I_{NaP}

Recombinant $\text{Na}_v1.6$ channels generate a conspicuous persistent Na^+ current (I_{NaP}) component (Rush et al. 2005), and published data suggest that these subunits underlie a significant proportion of I_{NaP} in different neuronal cell types (Do and Bean 2004; Maurice et al. 2001). Ramp commands (50 mV/s) applied to CA1 pyramidal neurons recorded in hippocampal slices (Fig. 4Aa) revealed a prominent inward current corresponding to I_{NaP} that was blocked by application of 1 μM TTX (Fig. 4Ab). I_{NaP} was isolated by subtracting recordings in the presence of TTX from control recordings (Fig. 4A, c and d, for *Scn8a^{wt}* and *Scn8a^{med}* mice, respectively). The maximal I_{NaP} conductance was 1.9 ± 0.1 nS in *Scn8a^{wt}* neurons ($n = 11$) and 1.1 ± 0.2 nS in *Scn8a^{med}* neurons ($n = 16$), corresponding to a reduction of I_{NaP} in the latter group to 58.1% of wild-type levels ($P = 0.01$, Fig. 4B). At the same time, the voltage-dependence of I_{NaP} was similar in the two groups (Fig. 4C; *Scn8a^{wt}* neurons: $V_{1/2} = -38.6 \pm 2.4$ mV and $k_m = 4.1 \pm 0.3$

mV, $n = 11$; *Scn8a^{med}* neurons: $V_{1/2} = -39.8 \pm 1.3$ mV and $k_m = 3.4 \pm 0.3$ mV, $n = 16$, $P > 0.05$).

Absence of $\text{Na}_v1.6$ reduces resurgent Na^+ currents I_{NaR}

$\text{Na}_v1.6$ subunits have been shown to contribute to resurgent Na^+ (I_{NaR}) in expression systems (Smith et al. 1998) and cerebellar neurons (Raman et al. 1997). We first tested whether I_{NaR} is present in CA1 neurons of *Scn8a^{wt}* mice. Following inactivation of Na^+ currents during a 15-ms prepulse to 20 mV, repolarization with a test pulse to various potentials from -100 to -10 mV gave rise to a resurgent current component within the voltage range of -50 to -10 mV (Fig. 5A, current trace at test pulse of -30 mV, in *Scn8a^{wt}* mouse). The magnitude of the resurgent current I_{NaR} was assessed by subtracting the steady-state current component at the end of the test pulse (I_{ss}) from the peak of the test pulse current (Fig. 5A). Representative current families from *Scn8a^{wt}* and *Scn8a^{med}* mice are shown in Fig. 5B, a and b, respectively. The magnitude of the resurgent current I_{NaR} proved to be significantly smaller in *Scn8a^{med}* (-20.77 ± 4.1 pA, $n = 11$) compared with *Scn8a^{wt}* mice (-71.29 ± 17.04 pA, $n = 10$, $P < 0.01$, see Fig. 5C for cumulative probability plot of I_{NaR} amplitudes at -30 -mV test pulses, and Fig. 5D for mean values). The voltage dependence of I_{NaR} does not appear different when comparing both genotypes (Fig. 5E). These experiments indicate that $\text{Na}_v1.6$ subunits localized at the AIS generate resurgent currents in CA1 pyramidal cells.

Lack of compensatory changes in I_{CaT}

The loss of $\text{Na}_v1.6$ has been shown to lead to compensatory regulation of other subthreshold inward currents, notably T-type Ca^{2+} currents (I_{CaT}) in Purkinje cells (Swensen and Bean

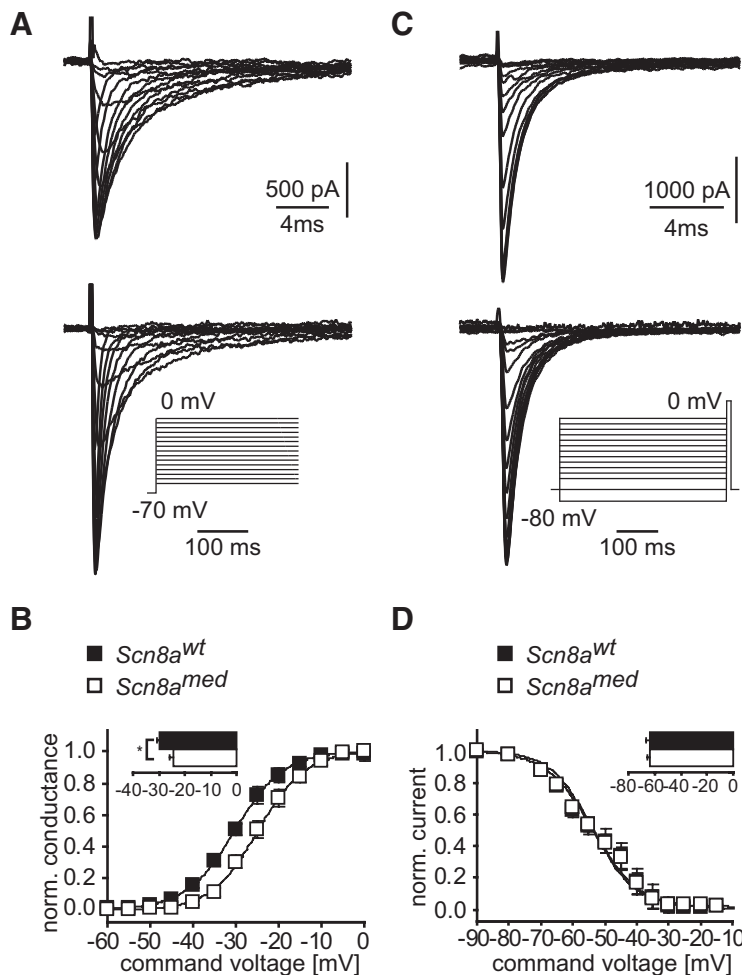


FIG. 3. The voltage dependence of activation of I_{NaT} in CA1 pyramidal neurons is shifted in a depolarizing direction in the absence of functional Na_v1.6 subunits. **A**: representative examples of I_{NaT} elicited in dissociated CA1 neurons from a *Scn8a*^{wt} (top) and a *Scn8a*^{med} mouse (bottom). The voltage paradigm is shown in the inset. **B**: voltage-dependent activation of I_{NaT} for *Scn8a*^{med} mice (□, $n = 7$) and *Scn8a*^{wt} littermates (■, $n = 6$). Data from individual cells were fitted with a Boltzmann function (see METHODS). Boltzmann functions constructed from the average values of $V_{1/2}$ and k_m are superimposed on the depicted data points. The voltage of half-maximal activation $V_{1/2}$ of I_{NaT} was significantly shifted to a more depolarized voltage in *Scn8a*^{med} mice (see inset, $P = 0.008$). **C**: voltage dependence of inactivation of I_{NaT} . Representative examples of I_{NaT} elicited in dissociated CA1 neurons from a *Scn8a*^{wt} (top) and a *Scn8a*^{med} mouse (bottom). The voltage paradigm is shown in the inset. **D**: the voltage dependence of inactivation was unchanged in *Scn8a*^{med} mice ($V_{1/2}$ in *Scn8a*^{wt} and *Scn8a*^{med} mice indicated in the inset, $P > 0.05$). Boltzmann functions superimposed on the data points as for **B**.

2005). We isolated I_{CaT} current pharmacologically in intact CA1 neurons in the slice preparation using a cocktail of Ca²⁺ channel blockers and TTX (see METHODS). T-type currents were discriminated on the basis of their slow deactivation kinetics in Ca²⁺ tail current recordings (Fig. 6A) (Sochivko et al. 2002). T-type current mediated tail current amplitudes in CA1 were not different at all tested command voltages (Fig. 6B). For instance, average maximal current amplitudes were -388.51 ± 55.9 pA in *Scn8a*^{med} ($n = 8$) and -373.30 ± 106.7 pA in *Scn8a*^{wt} neurons ($n = 7$).

Na_v1.6 contributes to setting spike threshold in CA1 pyramidal cells

The pronounced depolarizing shift in the voltage dependence of the transient Na⁺ current I_{NaT} predicts a depolarizing shift in spike threshold. To test this prediction, we performed whole cell current-clamp recordings in CA1 pyramidal cells in the slice preparation. Spikes were evoked by injecting brief (4 ms) depolarizing current pulses from a membrane potential of -80 mV imposed with slow current clamp (see METHODS, Fig. 7, A and B). Spike thresholds were significantly more depolarized in *Scn8a*^{med} compared with *Scn8a*^{wt} neurons (-56.7 ± 1.0 mV, $n = 14$ compared with -60.4 ± 0.9 mV; $n = 22$), respectively. This corresponds to a statistically significant 3.7 mV shift (Fig. 7C; $P = 0.011$). Changes of similar magnitude were also observed when spikes were elicited from

other holding potentials within the range of -65 to -80 mV (Fig. 7D), and, for instance, amounted to 4.9 mV for spikes elicited from -70 mV. We also measured other parameters of single spikes. When spikes were elicited by brief current injections, spike amplitude and the maximal rate of depolarization during spike upstroke were the same in the two groups of neurons (118.5 ± 0.4 mV and 419.6 ± 5.1 mV/ms in *Scn8a*^{wt} and 117.7 ± 0.7 mV and 405.9 ± 5.8 mV/ms in *Scn8a*^{med} neurons, $P > 0.05$), as expected from the lack of difference in maximal Na⁺ conductance. We did find a statistically significant, albeit small, increase in the maximal rate of spike repolarization in *Scn8a*^{med} versus *Scn8a*^{wt} neurons (-86.2 ± 1.9 vs. -78.2 ± 2.0 mV/ms, respectively, for spikes evoked from a holding potential of -80 mV; $P = 0.007$). The active spike afterdepolarization (spike ADP, see METHODS) was not different when comparing *Scn8a*^{wt} (168.3 ± 6.8 mV * ms, $n = 22$) and *Scn8a*^{med} neurons (149.3 ± 11.3 mV * ms, $n = 14$).

A difference in spike threshold was also found during repetitive neuronal firing elicited by prolonged (600 ms) depolarizing current pulses (Fig. 7, E and F). In these analyses of repetitive firing, the average current injection steps were larger for *Scn8a*^{med} compared with *Scn8a*^{wt} mice to account for the reduced gain (cf. Fig. 8). We analyzed the threshold for the first, second, third, and following spikes separately (Fig. 7G). This analysis also revealed a significantly more depolarized spike threshold in *Scn8a*^{med} mice. A potential confounding

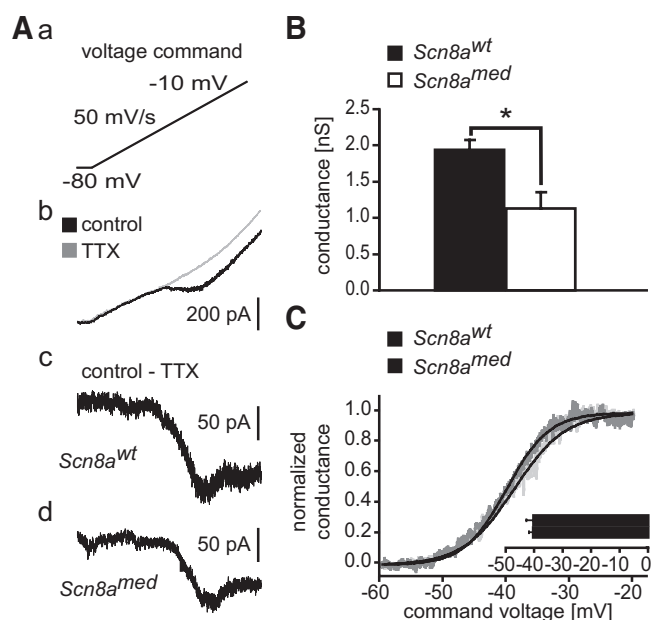


FIG. 4. Analysis of the persistent Na^+ current (I_{NaP}) in *Scn8a^{wt}* and *Scn8a^{med}* CA1 pyramidal neurons. **A**: in recording solutions designed to reduce other types of inward and outward currents (see METHODS), voltage ramps (50 mV/s, **a**) were applied to elicit I_{NaP} . **b**: current traces elicited under control conditions in an intact CA1 neuron in the slice preparation in a *Scn8a^{wt}* mouse in the absence (black trace) and presence of 0.5 μM TTX (gray trace). The TTX-sensitive I_{NaP} was isolated by subtraction (subtracted trace in **c**). A representative TTX subtracted I_{NaP} current trace recorded in a *Scn8a^{med}* neuron is depicted in (**d**). **B**: averaged peak conductances (see METHODS) obtained from neurons of *Scn8a^{wt}* and *Scn8a^{med}* mice ($n = 11$ and $n = 16$, respectively). I_{NaP} amplitude was reduced to 58.1% of wild-type littermate I_{NaP} amplitude in mutant mice ($P = 0.01$). **C**: the voltage dependence of activation of I_{NaP} was derived from current traces as depicted in **A**, **c** and **d** (see METHODS), and averaged for *Scn8a^{med}* (gray, $n = 16$) and *Scn8a^{wt}* neurons (light gray, $n = 11$). Superimposed fit curves were constructed from the averaged fit parameters derived for *Scn8a^{med}* (dark gray) and *Scn8a^{wt}* mice (black). Neither the voltage of half-maximal activation $V_{1/2}$ nor the slope factor k_m of I_{NaP} is significantly affected by the absence of functional $\text{Na}_v1.6$ channels ($P > 0.05$).

factor in this analysis is that the time of occurrence of spikes after onset of the current injection could be different between *Scn8a^{wt}* and *Scn8a^{med}* mice. However, except for the first spike in a train, which occurred significantly earlier after the onset of the current injection, the time points at which subsequent spikes occurred were not significantly different (Fig. 7H). The spike history was thus well comparable between genotypes using this form of analysis. An additional analysis in which spikes were binned according to the time of their occurrence after the onset of current injection (bin width: 100 ms) also yielded comparable results: thresholds in *Scn8a^{med}* neurons were significantly more positive than those of their *Scn8a^{wt}* counterparts for all bins (data not shown). Collectively, these results support the notion that the high-density of $\text{Na}_v1.6$ channels at the AIS contributes to its low spike threshold.

Na_v1.6 contributes to spike gain

Both the depolarizing shift in the spike threshold, as well as potentially the diminished resurgent Na^+ current (Raman and Bean 1997; Raman et al. 1997) would be expected to reduce the spike gain of CA1 neurons in *Scn8a^{med}* mice. We therefore tested whether spike gain is affected by applying prolonged (600 ms) depolarizing current pulses of increasing magnitude

(from 20 to 120 pA) and examining the number of spikes evoked by equivalent current injection steps in seven *Scn8a^{wt}* and 5 *Scn8a^{med}* neurons (Fig. 8, **A** and **B**, respectively). Indeed the relation of current injection to the corresponding spike frequency was significantly steeper in *Scn8a^{wt}* compared with *Scn8a^{med}* neurons ($P < 0.01$; Fig. 8C).

Na_v1.6 contributes to axonal spike initiation

Spike initiation occurs within the axon in most types of cortical neurons (Colbert and Pan 2002; Khaliq and Raman 2006; Palmer and Stuart 2006; Stuart and Hausser 1994; Stuart and Sakmann 1994; Stuart et al. 1997), and more precise attempts at localization have revealed an initiation site at the most distal portion of the AIS in layer 5 cortical pyramidal neurons (Palmer and Stuart 2006) and CA3 pyramidal neurons (Meeks and Mennerick 2007). In action potentials elicited by prolonged current injection, phase plots (dV/dt vs. V) allowed to distinguish a first phase of spike upstroke due to spike propagation from the AIS into the soma (McCormick et al. 2007; Shu et al. 2007), and a second phase, caused by the somatic spike (Fig. 9, **A** and **B**). This phenomenon was observed both for the first spike as well as for spikes occurring later during prolonged (600 ms) current injections (Fig. 9, **A**: 1st spike in train; **B**: 5th spike in train, multiple spikes from individual cells are shown). The initiation of spikes in *Scn8a^{wt}* neurons ($n = 7$; Fig. 9, **A** and **B**, top traces) appeared more abrupt than in *Scn8a^{med}* mice ($n = 5$; Fig. 9, **A** and **B**, bottom traces). This abrupt initiation was previously described in neocortical neurons as “kink” and is a consequence of the invasion of the soma by an axonal spike (McCormick et al. 2007; Shu et al. 2007). The “abruptness” of the voltage change at the onset of a spike can be quantified as a maximum of the second derivation of the voltage trace. We calculated the second derivation of the voltage traces (see Coombs et al. 1957); voltage recordings in Fig. 10, **Aa** and **Ba**, first and second derivation in **Ab** and **Bb**, second derivation depicted in gray, corresponding to the rate of change of dV/dt , in which a first (axonal) component and the second (somatic) component could be discriminated (Fig. 10, **Ab** and **Bb**). When this analysis was performed, the amplitude of the first peak in the second derivation of the voltage traces was significantly smaller in *Scn8a^{med}* neurons, regardless of which spike in a train was evaluated (Fig. 10C, comparable results obtained when action potentials were binned into 100-ms bins according to the time of occurrence after onset of the current injection, data not shown), reflecting the less abrupt rise of the voltage trace at the initiation of spikes seen in the phase plots (see Fig. 9, **Ab** and **Bb**).

As the two consecutive peaks in the second derivation of the voltage trace reflect axonal and somatic spike initiation, the delay between them (t_{del}) is a measure of the time from the initiation of the action potential at the AIS and its arrival at the soma. We examined how t_{del} varied during repetitive spiking evoked by prolonged (600 ms) depolarizing current pulses. For this analysis, we again analyzed the first, second, and subsequent spikes separately. We found that t_{del} was significantly larger in *Scn8a^{med}* compared with *Scn8a^{wt}* mice ($P < 0.01$, comparisons of individual datapoints with t -test indicated by asterisks in Fig. 10D). The lack of difference for the first spike in a train may be related to the different latency

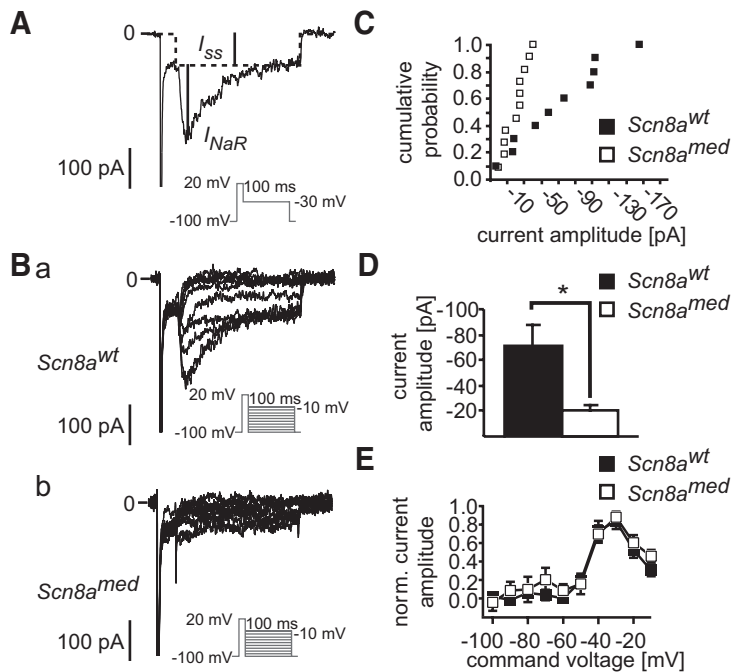


FIG. 5. Analysis of the resurgent Na⁺ current (I_{NaR}) in acutely dissociated *Scn8a*^{wt} and *Scn8a*^{med} CA1 pyramidal neurons. **A**: in recording solutions designed to reduce other types of inward and outward currents, I_{NaR} amplitude was assessed by subtracting the steady-state current (I_{ss}) at the end of the 100-ms test pulse (voltage protocol see inset) from the peak current. **B**: family of current traces elicited by test pulses ranging from -100 to -10 mV in a *Scn8a*^{wt} (*Ba*, $n = 10$) and *Scn8a*^{med} (*Bb*, $n = 11$). **C**: cumulative probability plot of I_{NaR} amplitude elicited with a test pulses to -30 mV in *Scn8a*^{wt} (■) and *Scn8a*^{med} (□). **D**: averaged peak amplitudes of I_{NaR} obtained from neurons of *Scn8a*^{wt} and *Scn8a*^{med} mice. I_{NaR} amplitude was reduced to 29.1% of wild-type littermate I_{NaR} amplitude in mutant mice ($P < 0.01$). **E**: averaged voltage dependence of normalized I_{NaR} recorded in *Scn8a*^{wt} (■) and *Scn8a*^{med} (□) neurons appears unchanged ($P > 0.05$).

of occurrence after onset of the current injection for the first spike only (see Fig. 7H). Comparable results were obtained when spikes were binned into 100-ms bins according to the time of occurrence after onset of the current injection (significantly longer t_{del} for all except the initial bin, data not shown). This type of analysis was not performed for single spikes elicited with 4-ms current injections because the spike upstroke was strongly contaminated to different degrees in different cells by the artifact induced by the current injection step.

Computer simulations of spike initiation at the AIS

Our electrophysiological results described above strongly suggest that in CA1 pyramidal cells, the high density of Na_v1.6 channels imposes a low spike threshold at the AIS so that spikes are initiated in this region before they appear in the soma. Another factor that may influence spike threshold and spike trigger zone is the overall density of Na⁺ channels at the AIS compared with that at the soma. Studies using cell-attached patch-clamp recordings to compare I_{NaT} densities at

AIS versus soma membranes have reported either equal densities (Colbert and Johnston 1996; Colbert and Pan 2002) or a much higher densities at the AIS (Kole et al. 2008). To explore the consequences of systematically altering I_{NaT} density and/or its voltage dependence on spike threshold and trigger zone, we performed simulations in a realistic computer model of a CA1 neuron (see Fig. 11C for morphology; see METHODS for detailed description of conductances). This approach also allowed us to directly compare voltage traces at axonal and somatic sites. The incorporated in this model is shown in Fig. 11A (see METHODS for parameters). This current was incorporated in the axonal and somatic compartments. We then varied the voltage of half-maximal activation ($V_{1/2}$) systematically at the AIS, such that it was ≤ 7 mV more hyperpolarized than at the soma ($\Delta V_{1/2}$: shift of $V_{1/2}$ of activation relative to somatic i_{NaT} , activation curves are depicted for $\Delta V_{1/2}$ of 0, -4 and -7 mV shown in Fig. 11B). As a second parameter, we varied i_{NaT} density at the AIS. Figure 11D shows exemplary somatic spikes elicited by brief current injection at the soma of the model neuron (i_{NaT} densities at the AIS and at the soma were equal; $\Delta V_{1/2}$ was 0 and -7 mV, as indicated, detailed description of spike properties for different i_{NaT} densities and $\Delta V_{1/2}$ in Supplementary Fig. S2).¹

We then simulated the model neuron with brief current injections recording the voltage responses in both the AIS (gray) and the soma (black) of the model neuron (Fig. 12A), while varying $\Delta V_{1/2}$ (0 to -7 mV) and i_{NaT} density at the AIS (from 0.02 to 1 S/cm², corresponding to a 0.2- to 10-fold difference in i_{NaT} density relative to the somatic i_{NaT} density of 0.1 S/cm²). The axo-somatic delay was then calculated as the delay between the time points at which the slope of rise in both compartments was maximal. A delay could also be derived from somatic voltage traces alone in our model, similar to the in vitro recordings. Derivations of simulated somatic voltage traces also revealed two distinct peaks under most conditions.

¹ The online version of this article contains supplemental data.

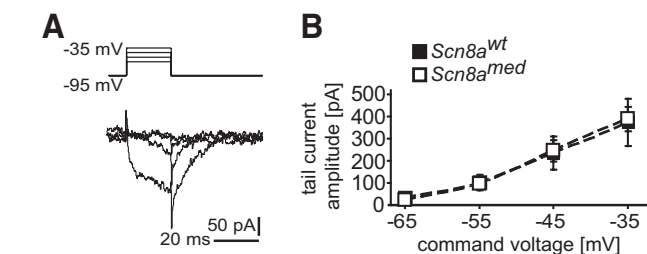


FIG. 6. T-type Ca²⁺ (I_{CaT}) current amplitude is unaltered in CA1 pyramidal cells of *Scn8a*^{med} mice. **A**: Ca²⁺ currents were elicited under recording conditions designed to block Na⁺ and K⁺ currents and to maximize the contribution of I_{CaT} to the inward currents (see METHODS for exact description). Under these conditions, compound Ca²⁺ tail currents consisting mainly of R- and T-type currents were elicited following brief depolarizations, with the slow component reflecting I_{CaT} (20 ms, voltage protocol see inset). **B**: the amplitude of I_{CaT} was not different in *Scn8a*^{med} ($n = 8$) compared with *Scn8a*^{wt} ($n = 7$) mice at any of the command voltages ($P > 0.05$).

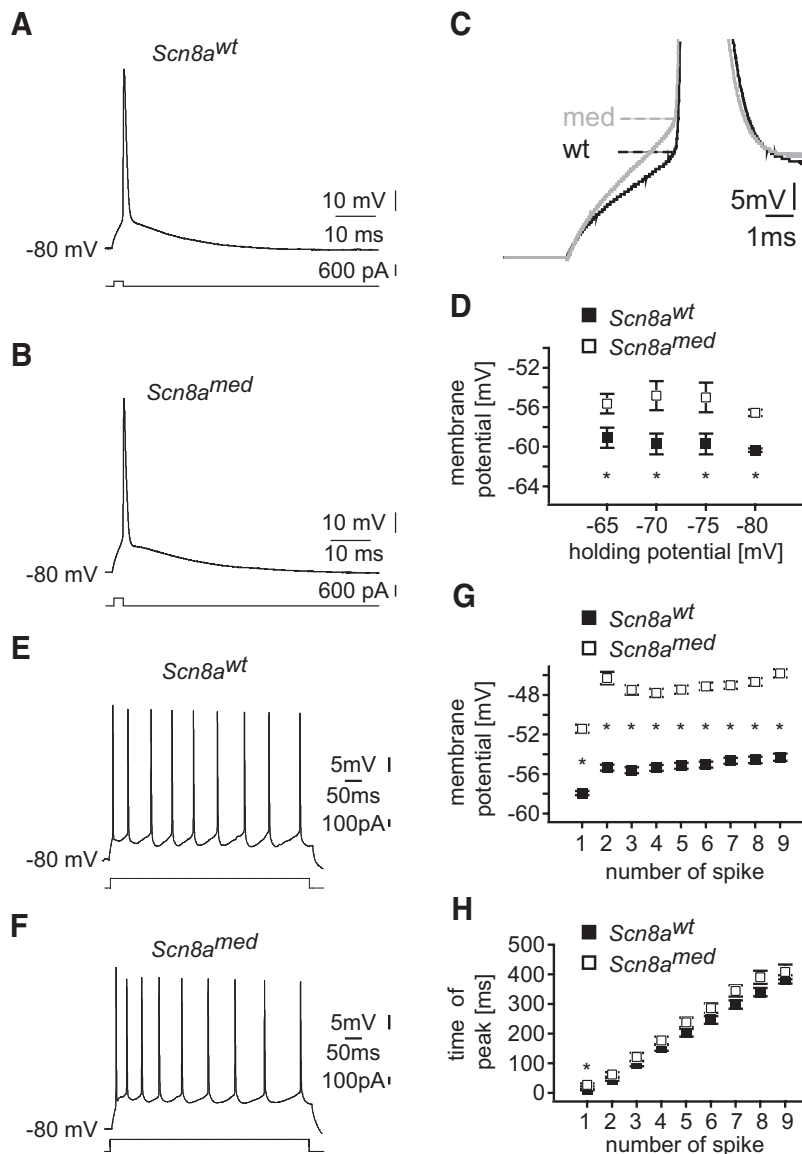


FIG. 7. Spike threshold of intact CA1 pyramidal neurons recorded in the slice preparation is increased in *Scn8a^{med}* mice. A and B: example traces of spikes elicited by brief (4 ms) just suprathreshold current injection recorded in a *Scn8a^{wt}* (A) or *Scn8a^{med}* mouse (B). Bottom traces: the corresponding current injection. Slow current clamp was used to set the membrane potential to -80 mV. C: overlay of the 2 representative traces shown in A and B at higher magnification to illustrate the difference in spike threshold more clearly (gray trace: *Scn8a^{med}*). D: average values obtained for the spike threshold with short current injections (cf. A and B) in *Scn8a^{med}* (open symbols, *n* = 14) and *Scn8a^{wt}* mice (closed symbols, *n* = 22). The difference in threshold was significant at all membrane potentials given (asterisks, *P* < 0.05). E and F: example traces of spikes elicited with prolonged current injection (600 ms). G: average values for spike thresholds obtained during prolonged current injections (cf. E and F). The 1st 9 spikes were analyzed binned according to their spike history. As for brief current injections, the spike thresholds were significantly different between genotypes within all bins (*P* < 0.05). H: average values for the time of spike occurrence following the current injection according to spike history. Only the 1st spikes elicited occurred significantly later in *Scn8a^{med}* neurons (1st spike *P* < 0.05, subsequent spikes *P* > 0.05).

The values of the axo-somatic delay obtained in this manner from the somatic recording alone showed a strong linear correlation to the values derived as a delay between AIS and somatic spikes ($R^2 = 0.9388$).

When i_{NaT} densities at both soma and AIS were equal as suggested until recently (Colbert and Johnston 1996; Colbert and Pan 2002), spike initiation was strongly dependent on $\Delta V_{1/2}$. A pronounced delay from axonal to somatic spike initiation was observed at values of $\Delta V_{1/2}$ from -7 to -4 mV. When $\Delta V_{1/2}$ was reduced further, the axo-somatic delay showed a steep reduction (examples for $\Delta V_{1/2}$ of 0 and -7 mV in Fig. 12A*b*, results for all values of $\Delta V_{1/2}$ in Fig. 12B*a*, gray data points). A higher i_{NaT} density at the AIS as suggested by Kole et al. (2008) (≤ 10 -fold increase relative to the soma implemented in our model) always led to a spike initiation at the AIS, and a stereotypical axo-somatic delay of ~ 0.15 ms, irrespective of $\Delta V_{1/2}$ (Figs. 12A*c* and 9B*a*, black symbols). Conversely, a reduced i_{NaT} density at the AIS (0.2-fold of somatic i_{NaT} density) caused the spike to arise almost simultaneously in both compartments for all values of $\Delta V_{1/2}$ (Fig.

12, A*a* and B*a*, open symbols). Thus a $\Delta V_{1/2}$ of more than -4 mV strongly promotes spike initiation at the AIS, even when the i_{NaT} densities at the AIS and soma were uniform. This phenomenon was also clear when we plotted the axo-somatic delay versus the relative i_{NaT} density at the AIS (Fig. 12C*a*). This analysis revealed that for $\Delta V_{1/2}$ of 0 mV, the axo-somatic delay increased gradually with an increasing density of axonal i_{NaT} . When $\Delta V_{1/2}$ was increased, this relation began to show a steeper increase. As a consequence, a $\Delta V_{1/2}$ of -4 to -7 mV strongly affected spike initiation site over a wide range of AIS Na^+ channel density ratios (from ~ 0.5 -fold to 3-fold somatic density, Fig. 12C*a*).

The voltage dependence of activation of i_{NaT} at the AIS also influenced spike threshold as observed experimentally. When i_{NaT} densities at the AIS and soma were equal, the firing threshold was dependent on $\Delta V_{1/2}$, such that an increase in $\Delta V_{1/2}$ led to a more hyperpolarized spike threshold (examples for $\Delta V_{1/2}$ of 0 and -7 mV in Fig. 12A*b*, results for all values of $\Delta V_{1/2}$ in Fig. 12B*b*, gray data points). At a very high i_{NaT} density at the AIS, spike threshold was always hyperpolarized,

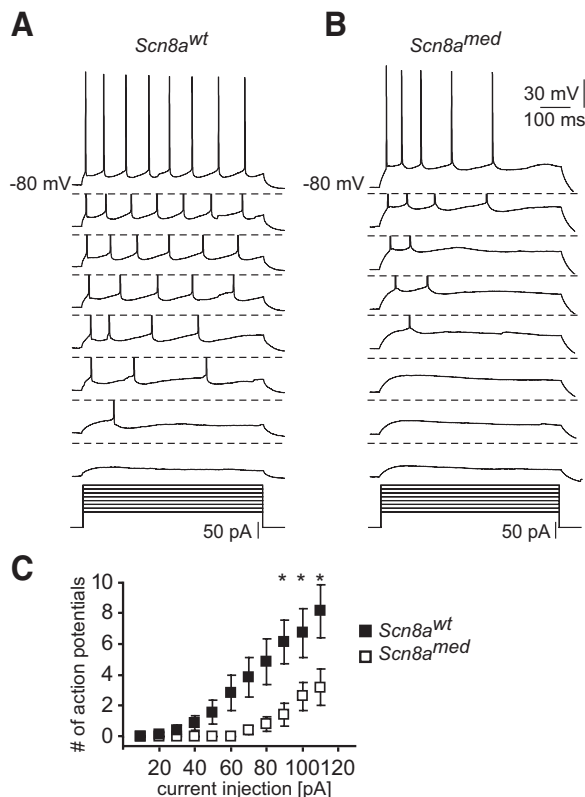


FIG. 8. Gain of CA1 neurons is decreased in the absence of Na_v1.6 channels. *A* and *B*: example traces of spikes elicited by current injections (600 ms) of increasing magnitude from a holding potential of -80 mV. Some traces are truncated at -45 mV (---). Spike frequencies increase in both *Scn8a*^{wt} and *Scn8a*^{med} mice, but the increase is considerably less pronounced in *Scn8a*^{med} mutant mice. *C*: quantification of the significant difference between genotypes in gain of CA1 neurons by plotting the number of spikes during the 600-ms current injection vs. the magnitude of the current injection (*Scn8a*^{wt}, $n = 7$ and *Scn8a*^{med}, $n = 5$, $P < 0.01$).

irrespective of $\Delta V_{1/2}$ (Fig. 12, *Ac* and *Bb*, black symbols). Conversely, very low i_{NaT} density at the AIS led to a depolarized spike threshold without dependence on $\Delta V_{1/2}$ (Fig. 12, *Aa* and *Bb*, open symbols).

In *Scn8a*^{med} mice, we observed a significant reduction of I_{NaP} and I_{NaR} current. Of these two current components, I_{NaP} might conceivably contribute to action potential initiation. We have therefore repeated the modeling experiment with i_{NaP} reduced to 60% in all compartments in which it was present (soma: reduction to 0.6 mS/cm², AIS: 0.3 mS/cm², Fig. 13). In additional experiments, we reduced i_{NaP} only at the AIS (Supplementary Fig. S1). Under both conditions, the impact of varying i_{NaT} was similar to those depicted in Fig. 12. In both cases, changing the voltage dependence of activation of i_{NaT} at the AIS still influenced the axo-somatic delay (Fig. 13*Aa* and Supplementary Fig. S1*Aa*) and spike threshold (Fig. 13*Ab* and Supplementary Fig. S1*Ab*). Varying the density of i_{NaT} at the AIS also caused changes in axo-somatic delay and spike threshold that were well comparable to the data obtained without reduction in i_{NaP} (Fig. 13*B* and Supplementary Fig. S1*B*, cf. Fig. 12*C*).

DISCUSSION

The main conclusion from our electrophysiological and immunohistochemical experiments is that Na_v1.6 channels are

aggregated at the AIS of hippocampal pyramidal neurons, where they are responsible for the hyperpolarized voltage-dependence of activation of I_{NaT} . Furthermore, Na_v1.6 subunits also contribute to persistent and resurgent Na⁺ currents in CA1 pyramidal neurons. Through their unique biophysical properties and concentration at the axon initial segment, Na_v1.6 subunits contribute to localization of the spike trigger zone to the AIS.

Regarding spike initiation, two major changes were observed in *Scn8a*^{med} mice. First we observed a significant depolarizing shift in spike threshold in mice lacking Na_v1.6 channels. In addition, deletion of Na_v1.6 channels from the AIS significantly reduced the temporal separation between axonal and somatic components of spike initiation in repetitive firing. Previous studies have shown that spike initiation occurs within the distal portion of the AIS in cortical neurons (Meeks and Mennerick 2007; Palmer and Stuart 2006) or the first node of Ranvier in Purkinje neurons (Clark et al. 2005). Interplay between several factors likely endows these subcellular compartments with a particularly low spike threshold. First the passive electrical properties of axon versus soma may play an important role. Modeling and physiological studies suggest that charging of the AIS capacitance by inward current is rapid with the much larger somatic capacitance being charged with a significant delay (McCormick et al. 2007; Meeks and Mennerick 2007; Shu et al. 2007). Second, a high density of AIS Na⁺ channels was suggested to subserve AIS spike initiation in modeling and electrophysiological studies. Several studies have shown a high density of Na⁺ channel proteins at the AIS (Boiko et al. 2001, 2003; Catterall 1981; Hossain et al. 2005; Pan et al. 2006; Van Wart and Matthews 2006), but how far this correlates with AIS Na⁺ current density is a matter of current debate (Colbert and Pan 2002; Kole et al. 2008; Palmer and Stuart 2006). Finally, the more negative activation voltages of AIS Na⁺ channels are thought to lower spike threshold (Colbert and Pan 2002). Clearly these factors are not mutually exclusive; rather, it is likely that these three factors in combination localize the spike trigger zone to the AIS. The most likely interpretation of the reduced axo-somatic delay in our view is that the site of spike initiation is located closer to the soma. This is also suggested by the modeling data, where removing the voltage shift of I_{NaT} caused a simultaneous spike initiation in soma and AIS (cf. Fig. 12*Ab*, equal density of I_{NaT} at AIS and soma).

In mice lacking the AIS Na⁺ channel subunit Nav1.6, we found a pronounced depolarizing shift in the half-maximal activation of I_{NaT} in CA1 neurons. This finding is consistent with studies that have examined the properties of Na_v1.2 or Na_v1.6 channels by overexpressing them in mammalian cells. These experiments have indicated that the activation curve of Na_v1.6 channels is shifted in a hyperpolarized direction compared with Na_v1.2 (Rush et al. 2005). It should be noted that such a shift was not observed when Na_v subunits were expressed in oocytes, for unknown reasons (Smith et al. 1998). A shift in the voltage dependence of activation was also not observed in globus pallidus neurons (Mercer et al. 2007), cerebellar neurons (Raman et al. 1997) or mesencephalic trigeminal neurons (Enomoto et al. 2007) from *Scn8a*^{med} mice. Regarding the voltage-dependence of inactivation, a more hyperpolarized voltage dependence of I_{NaT} was observed for Na_v1.6 channels compared with Na_v1.2 channels (Rush et al.

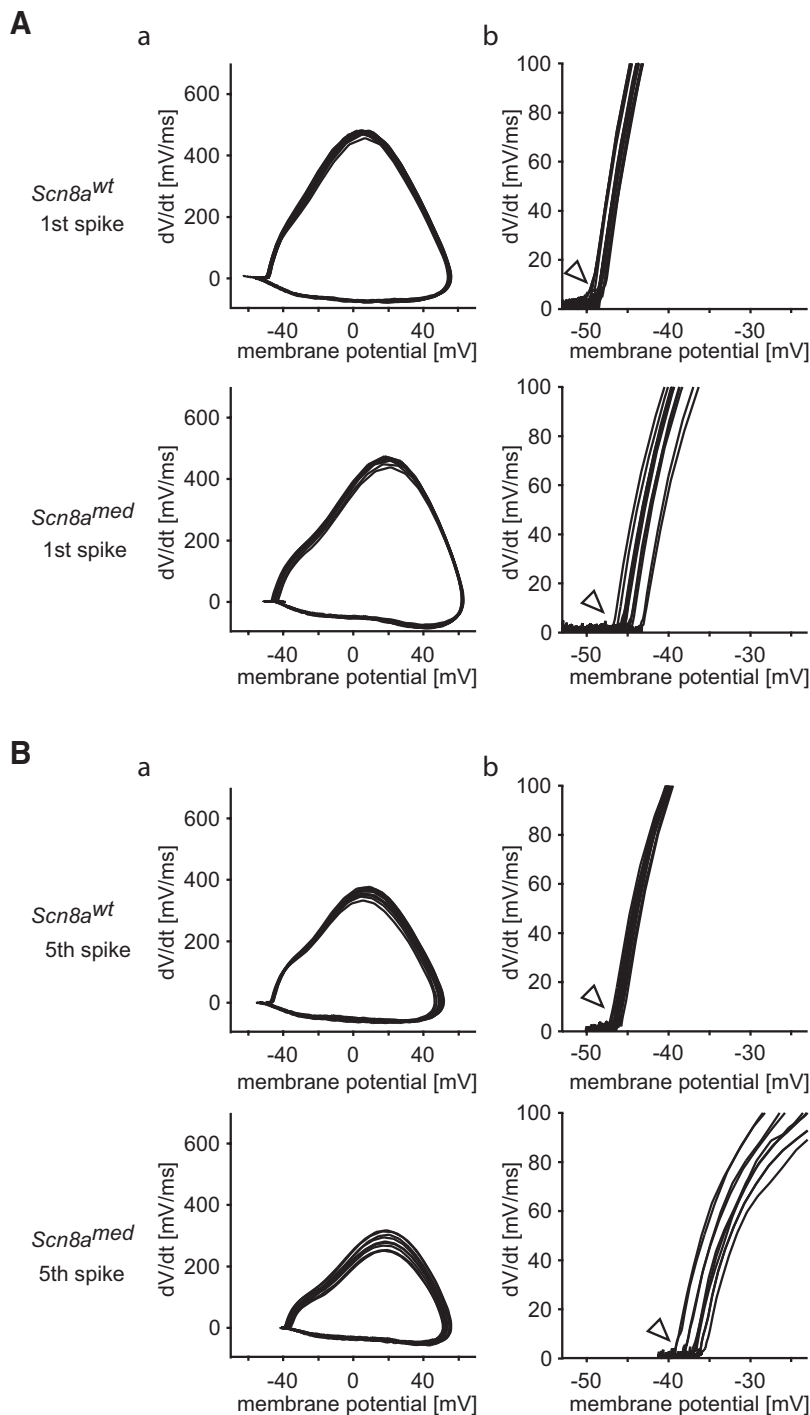


FIG. 9. Spike initiation in *Scn8a^{wt}* and *Scn8a^{med}* mice. Phase plots of dV/dt vs. V for all the 1st (*Aa*) and 5th (*Ba*) spikes generated in a *Scn8a^{wt}* (*top*) and a *Scn8a^{med}* neuron (*bottom*). Note the nonmonotonous ascending phase of the spikes, suggestive of 2 underlying components. *Ab* and *Bb*: sections of the corresponding phase plots representing spike initiation shown with higher resolution. Note the abrupt rise of dV/dt in *Scn8a^{wt}* ("kink," indicated by arrowheads, *Ab* and *Bb*, *top*) that is much less pronounced in *Scn8a^{med}* mice (*Ab* and *Bb* *bottom*).

2005), but no changes in this biophysical parameter were observed in different cell types in mice lacking functional $Na_v1.6$ channels (Enomoto et al. 2007; Mercer et al. 2007; and this study, but see Raman et al. 1997). The reasons for these disparate findings are currently unknown but may indicate both cell-specific regulation of $Na_v1.6$ channels as well as potential compensatory changes following loss of $Na_v1.6$ channels. Regardless of these discrepancies, our results indicate that in CA1 neurons, $Na_v1.6$ subunits contribute a Na^+ channel component that activates at more hyperpolarized voltages than the remainder of the cellular Na^+ currents. Our and published immunolabeling experiments

(Boiko et al. 2003; Garrido et al. 2003; Van Wart and Matthews 2006; Van Wart et al. 2007) indicate that these channels are located at the AIS of different types of principal neurons, suggesting that they may underlie biophysical specialization of AIS Na^+ channels (Colbert and Pan 2002). It should be noted, however, that our recordings of the biophysical properties of I_{NaT} in *Scn8a^{med}* and *Scn8a^{wt}* mice were performed in dissociated CA1 neurons, which may contain variable portions of axonal membrane. We cannot therefore exclude that $Na_v1.6$ channels at the AIS might have properties distinct from somatic $Na_v1.6$ channels, perhaps via specific interactions with AIS proteins (Shira-

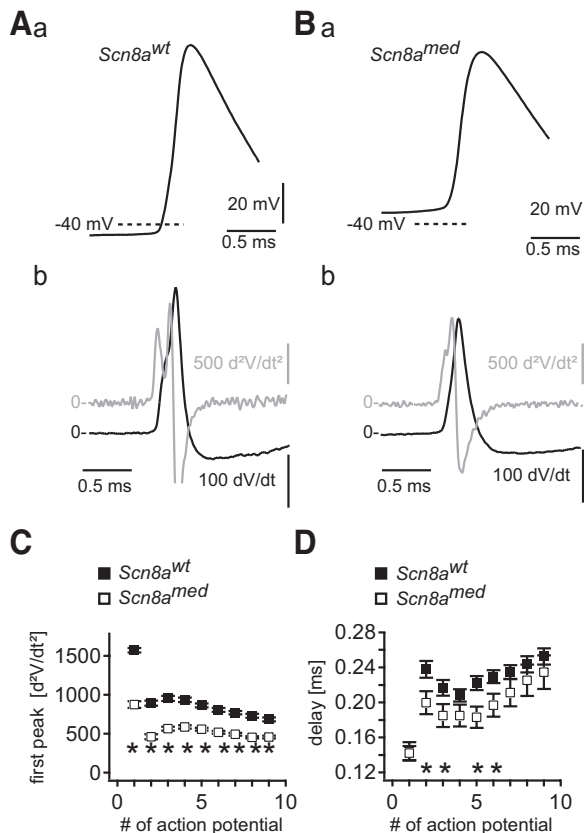


FIG. 10. Altered delay between axonal and somatic components and steepness of spike initiation. *Aa* and *Ba*: representative traces of a 5th spike from a *Scn8a*^{wt} (*A*) and *Scn8a*^{med} mouse (*B*). *Ab* and *Bb*: 1st and 2nd derivation of the voltage traces shown in *Aa* and *Ba*. The 2nd derivation is depicted in gray. Note the occurrence of 2 consecutive peaks in both cases, with a smaller temporal delay in the CA1 neuron from a *Scn8a*^{med} mouse. *C*: the amplitude of the 1st (axonal) peak in the second derivation of the voltage trace is significantly decreased in *Scn8a*^{med} mice, as expected from the less abrupt rise of the initial phase of the spike in *Scn8a*^{med} mutant compared with *Scn8a*^{wt} neurons (cf. Fig. 9, *Ab* and *Bb*, $P < 0.05$). *D*: quantitative determination of the delay between axonal and somatic component in *Scn8a*^{wt} and *Scn8a*^{med} mice (t_{del}). t_{del} was determined as the latency between the 1st and 2nd peak of the second derivation of the voltage traces. Spikes were binned depending on their spike history. The latency t_{del} was significantly shorter for the 2nd ($P = 0.02$), 3rd ($P = 0.04$), 5th ($P = 0.01$), and 6th ($P = 0.02$) spike analyzed in the spike train.

hata et al. 2006). Nevertheless, the most parsimonious explanation for our results is that Na_v1.6 channels with a hyperpolarized threshold of activation aggregate at the AIS.

We did not quantitatively assess if the density of Na⁺ channels at the AIS is altered in CA1 neurons and therefore cannot exclude a reduction in the overall density of AIS Na⁺ channels in *SCN8a*^{med} neurons. However, our immunohistochemical data suggest that there is no dramatic loss of AIS Na⁺ channels in these neurons. Relative to Ankyrin G as an AIS marker, we did not observe a reduction in PanNa_v immunolabeling in *Scn8a*^{med} neurons. This is similar to the results reported by van Wart et al. (2006), indicating a compensation of the loss of Na_v1.6 subunits at the AIS by other subunits, in particular Na_v1.2. A mild reduction in Na⁺ channel density might not be detected using immunolabeling, but would be unlikely to exclusively account for the observed changes in spike initiation.

Our modeling data allowed us to further address the interplay of the density and the voltage dependence of AIS Na⁺ channels in spike initiation. We show that a hyperpolarized voltage dependence of AIS Na⁺ currents influences spike initiation over a wide range of AIS Na⁺ channel densities (from ~0.5- to 3-fold of somatic density). If the density of Na⁺ channels at the AIS becomes even higher, the initiation site is less affected by the biophysical properties of these channels. The threshold for generation of a spike was differently affected by altering AIS Na⁺ channels. In this case, even at very high AIS Na⁺ channel densities ($\leq 10\times$ somatic density), a shift in voltage-dependent Na⁺ channel activation still influenced spike threshold (see Fig. 11*Cb*). At the same time, increasing the density of AIS channels always led to a more hyperpolarized somatic spike threshold. Thus the effects of varying the voltage dependence of AIS Na⁺ channels on spike threshold and spike trigger zone were robust over a large range of AIS Na⁺ current densities. These data indicate that the biophysical properties of AIS I_{NaT} are an important determinant of spike threshold and are consistent with the view that the voltage dependence of AIS Na_v1.6 is an important factor in spike initiation of CA1 pyramidal neurons. In addition to the changes in I_{NaT} , we also found a reduction of I_{NaP} in *Scn8a*^{med} mice. It is conceivable that Na_v1.6-mediated I_{NaP} could, by virtue of its hyperpolarized threshold of activation, contribute to spike initiation. However, modeling experiments showed that the influence of this current component on spike threshold and axo-somatic delay is likely to be much smaller than the influence of I_{NaT} .

The changes in I_{NaP} (by 41%) and I_{NaR} (by 69.2%) we observed in *Scn8a*^{med} mice are similar to the results reported

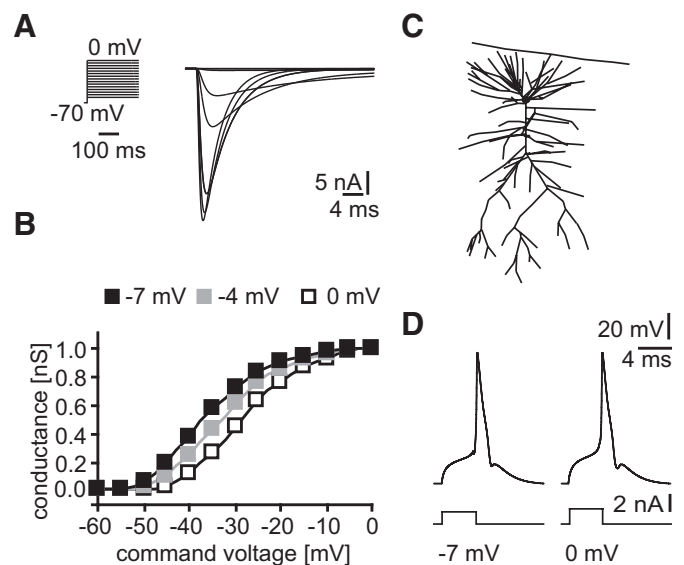


FIG. 11. Voltage dependence of activation of i_{NaT} and properties of the CA1 neuron model. *A*: characterization of i_{NaT} incorporated in the model. Na⁺ currents were simulated in an isopotential compartment and elicited with the voltage paradigm shown in the inset for $\Delta V_{1/2}$ of 0 mV. *B*: voltage dependence of activation of i_{NaT} for different values of $\Delta V_{1/2}$. Activation curves were constructed as described in METHODS. *C*: morphology of the modeled CA1 pyramidal neuron (see METHODS for detailed description). *D*: 2 simulated spikes with shifted voltage dependence of activation of axonal i_{NaT} elicited by brief (4 ms) somatic current injections. Leftmost trace: $\Delta V_{1/2}$ was -7 mV. Rightmost: $\Delta V_{1/2}$ was 0 mV, thus the voltage dependence of somatic and AIS currents was identical.

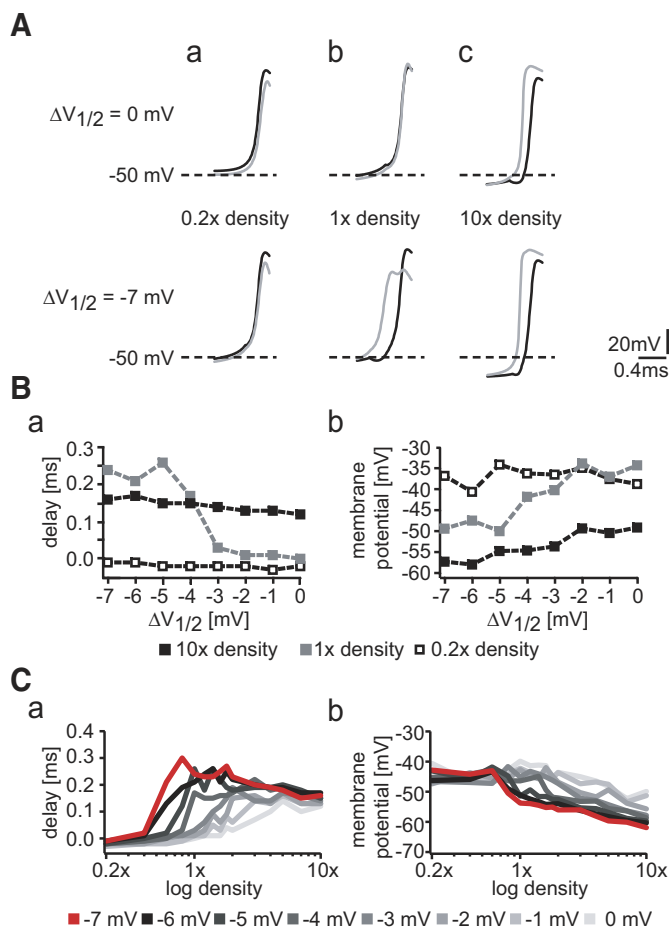


FIG. 12. Influence of transient AIS Na^+ current density and voltage dependence on spike initiation. *A*: the rising phase of axonal (gray) and somatic (black) spikes are depicted at high resolution either with $\Delta V_{1/2}$ of 0 mV (top traces) or -7 mV (bottom traces), for AIS Na^+ current densities of 0.2-, 1-, and 10-fold somatic density (*a-c*, respectively). *B*: plot of the delay between time of maximal rise in the AIS and somatic spike over $\Delta V_{1/2}$ for different AIS Na^+ current densities (*a*). An equivalent graph is shown for the spike threshold (*b*). *C*: illustration of the dependence of the axo-somatic delay on the density of axonal Na^+ current for different values of $\Delta V_{1/2}$ (see legend, *a*). An equivalent diagram is shown for the spike threshold (*b*).

for mesencephalic trigeminal neurons in $\text{Na}_v1.6$ null mice (39% reduction in I_{NaP} , 76% reduction in I_{NaR}) (Enomoto et al. 2007), DRG neuron cultures (complete ablation of I_{NaR}) (Cummins et al. 2005), subthalamic nucleus neurons (63% reduction in I_{NaR} , 55% reduction in I_{NaP}) (Do and Bean 2004), or cerebellar neurons (Raman and Bean 1997). Globus pallidus neurons in mice lacking $\text{Na}_v1.6$, surprisingly, show no reduction in I_{NaP} , but I_{NaR} is reduced (Mercer et al. 2007). Taken together, these results suggest that a significant portion of I_{NaP} and I_{NaR} is mediated by axonal $\text{Na}_v1.6$ channels. In addition to these neuron types in the cerebellum, diencephalon and brain stem, the presence of I_{NaR} was also reported in cortical pyramidal neurons of the perirhinal and entorhinal cortex, as well as in dentate granule cells and CA1 pyramidal neurons of ventral hippocampus (Castelli et al. 2007a,b). Both I_{NaR} and I_{NaP} mediated by $\text{Na}_v1.6$ have been shown to affect repetitive firing and spike output gain (Levin et al. 2006; Mercer et al. 2007; Raman et al. 1997). In addition, the changes in spike threshold would also be expected to have a similar effect. Indeed we also found a large reduction in spike output gain in

Scn8a^{med} compared with *Scn8a^{wt}* mice. It is likely that the changes in I_{NaR} , I_{NaP} , and I_{NaT} conspire in CA1 neurons to produce changes in output gain. These results are also interesting because they imply that a substantial portion of I_{NaP} and I_{NaR} may be generated at the AIS of different types of central neurons, as shown with physiological techniques (Astman et al. 2006; Castelli et al. 2007a).

I_{NaP} has also been shown to contribute strongly to spike afterdepolarizations in CA1 pyramidal neurons from adult animals (Yue et al. 2005). In young animals comparable to the age range employed in this study, not only I_{NaP} but also dendritic voltage-gated Ca^{2+} currents strongly amplify spike afterdepolarizations and cause the generation of spike bursts (Chen et al. 2005). In this age range, blocking either voltage-gated Ca^{2+} currents at the dendrites or I_{NaP} in the perisomatic region pharmacologically reduces spike afterdepolarizations and associated burst discharges. Surprisingly, spike afterdepolarizations were not reduced in *Scn8a^{med}* mice despite a reduction of I_{NaP} by 41.9%. One explanation for this unexpected finding might be that a partial reduction of I_{NaP} in young animals is not sufficient to affect the magnitude of the spike afterdepolarization, given the important contribution of voltage-gated Ca^{2+} currents at this age (Chen et al. 2005). An alternative explanation would be compensatory regulation of other voltage-gated ion channels occurring as a consequence of the constitutive lack of function of $\text{Na}_v1.6$. Indeed, functional deletion of $\text{Na}_v1.6$ in *Scn8a^{med}* mice causes compensatory upregulation of T-type Ca^{2+} channels in Purkinje neurons (Swensen and Bean 2005). In contrast, changes in K^+ channels were subtle, with only small changes in the voltage dependence of K^+ currents highly sensitive to TEA in *Scn8a^{med}* mice (Khaliq et al. 2003). We did not find a compensatory upregulation of T-type Ca^{2+} channels, indicating that different compensatory changes may be invoked in different neuron types.

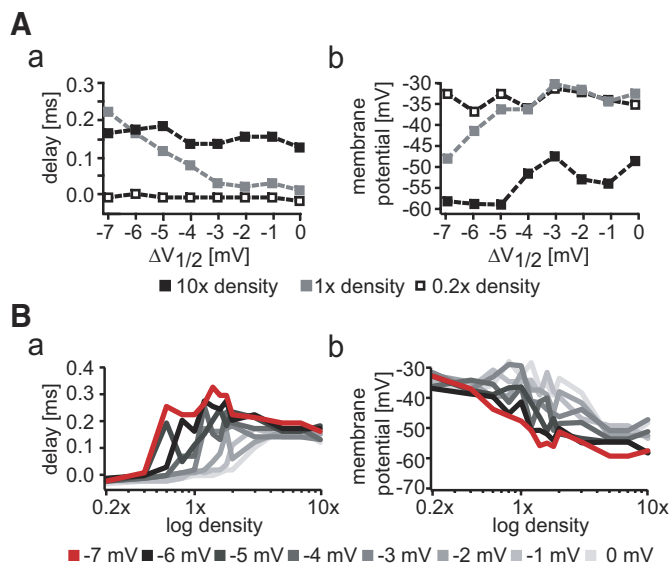


FIG. 13. Influence of transient AIS Na^+ current density and voltage dependence on spike initiation with a 60% reduction of persistent Na^+ current. *A*: plot of the delay between time of maximal rise in the AIS and somatic spike over $\Delta V_{1/2}$ for different AIS Na^+ current densities (*a*). An equivalent graph is shown for the spike threshold (*b*). *B*: illustration of the dependence of the axo-somatic delay on the density of axonal Na^+ current for different values of $\Delta V_{1/2}$ (see legend, *a*). An equivalent diagram is shown for the spike threshold (*b*).

Taken together, our results indicate that the presence of Na_v1.6 endows AIS Na⁺ channels with a hyperpolarized voltage dependence of activation that is important for the low threshold for spike initiation at the AIS. Furthermore, axonal Na_v1.6 channels contribute to I_{NaP} and I_{NaR} . The contribution of Na_v1.6 to these three current components plays a significant role in regulating neuronal repetitive discharge behavior. Our findings may be pertinent to many other types of brain neurons because Na_v1.6 subunit aggregation at the AIS has been demonstrated in neocortical, subicular, and hippocampal pyramidal neurons (Van Wart and Matthews 2006 and this study), as well as in cochlear (Hossain et al. 2005), retinal ganglion (Boiko et al. 2003), and Purkinje cells (Van Wart and Matthews 2006). The role of Na_v1.6 in controlling neuronal firing behavior is consistent with the elevated seizure thresholds observed in heterozygous *Scn8a*^{med/wt} mice (Martin et al. 2007). This study also suggests that reduced function of *Scn8a* limits hyperexcitability in a mouse model of severe myoclonic epilepsy of infancy, suggesting a role for this gene as a disease modifier in epilepsy. This study further underscores the important role of Na_v1.6 channels in controlling neuronal excitability on a systems level.

GRANTS

This work was supported by SFB-TR3 funding (Project C2, C7) to H. Beck, Y. Yaari, M.-T. Horstmann, M. Royeck, and LE660/4-1 to M.-T. Horstmann of the Deutsche Forschungsgemeinschaft, the program for German-Israeli Cooperation in the Neurosciences of the Bundesministerium für Bildung und Forschung, Germany, and Ministry of Science, Israel, (Projekträger DLR) to Y. Yaari and H. Beck, a Mercator Guest Professorship of the Deutsche Forschungsgemeinschaft to Y. Yaari, Humboldt Foundation funding to S. Remy, and BONFOR.

REFERENCES

- Astman N, Gutnick MJ, Fleidervish IA. Persistent sodium current in layer 5 neocortical neurons is primarily generated in the proximal axon. *J Neurosci* 26: 3465–3473, 2006.
- Bannister NJ, Larkman AU. Dendritic morphology of CA1 pyramidal neurons from the rat hippocampus. I. Branching patterns. *J Comp Neurol* 360: 150–160, 1995.
- Boiko T, Rasband MN, Levinson SR, Caldwell JH, Mandel G, Trimmer JS, Matthews G. Compact myelin dictates the differential targeting of two sodium channel isoforms in the same axon. *Neuron* 30: 91–104, 2001.
- Boiko T, Van Wart A, Caldwell JH, Levinson SR, Trimmer JS, Matthews G. Functional specialization of the axon initial segment by isoform-specific sodium channel targeting. *J Neurosci* 23: 2306–2313, 2003.
- Burgess DL, Kohrman DC, Galt J, Plummer NW, Jones JM, Spear B, Meisler MH. Mutation of a new sodium channel gene, *Scn8a*, in the mouse mutant “motor endplate disease.” *Nat Genet* 10: 461–465, 1995.
- Carnevale NT, Hines M. In: *The NEURON Book*. Cambridge, UK: Cambridge Univ. Press, 2006.
- Castelli L, Biella G, Toselli M, Magistretti J. Resurgent Na⁺ current in pyramidal neurons of rat perirhinal cortex: axonal location of channels and contribution to depolarizing drive during repetitive firing. *J Physiol* 582: 1179–1193, 2007s.
- Castelli L, Nigro MJ, Magistretti J. Analysis of resurgent sodium-current expression in rat parahippocampal cortices and hippocampal formation. *Brain Res* 1163: 44–55, 2007b.
- Catterall WA. Localization of sodium channels in cultured neural cells. *J Neurosci* 1: 777–783, 1981.
- Chen S, Yue C, Yaari Y. A transitional period of Ca²⁺-dependent spike afterdepolarization and bursting in developing rat CA1 pyramidal cells. *J Physiol* 567: 79–93, 2005.
- Clark BA, Monsivais P, Branco T, London M, Hausser M. The site of action potential initiation in cerebellar Purkinje neurons. *Nat Neurosci* 8: 137–139, 2005.
- Colbert CM, Johnston D. Axonal action-potential initiation and Na⁺ channel densities in the soma and axon initial segment of subicular pyramidal neurons. *J Neurosci* 16: 6676–6686, 1996.
- Colbert CM, Pan E. Ion channel properties underlying axonal action potential initiation in pyramidal neurons. *Nat Neurosci* 5: 533–538, 2002.
- Coombs JS, Curtis DR, Eccles JC. The generation of impulses in motoneurons. *J Physiol* 139: 232–249, 1957.
- Coulter DA, Huguenard JR, Prince DA. Calcium currents in rat thalamocortical relay neurons: kinetic properties of the transient, low-threshold current. *J Physiol* 414: 587–604, 1989.
- Cummins TR, Dib-Hajj SD, Herzog RI, Waxman SG. Nav1.6 channels generate resurgent sodium currents in spinal sensory neurons. *FEBS Lett* 579: 2166–2170, 2005.
- Do MT, Bean BP. Sodium currents in subthalamic nucleus neurons from Nav1.6-null mice. *J Neurophysiol* 92: 726–733, 2004.
- Enomoto A, Han JM, Hsiao CF, Chandler SH. Sodium currents in mesencephalic trigeminal neurons from Nav1.6 null mice. *J Neurophysiol* 98: 710–719, 2007.
- Garrido JJ, Giraud P, Carlier E, Fernandes F, Moussif A, Fache MP, Debanne D, Dargent B. A targeting motif involved in sodium channel clustering at the axonal initial segment. *Science* 300: 2091–2094, 2003.
- Gasparini S, Migliore M, Magee JC. On the initiation and propagation of dendritic spikes in CA1 pyramidal neurons. *J Neurosci* 24: 11046–11056, 2004.
- Golomb D, Yue C, Yaari Y. Contribution of persistent Na⁺ current and M-type K⁺ current to somatic bursting in CA1 pyramidal cells: combined experimental and modeling study. *J Neurophysiol* 96: 1912–1926, 2006.
- Halliwel JV, Adams PR. Voltage-clamp analysis of muscarinic excitation in hippocampal neurons. *Brain Res* 250: 71–92, 1982.
- Hamann M, Meisler MH, Richter A. Motor disturbances in mice with deficiency of the sodium channel gene *Scn8a* show features of human dystonia. *Exp Neurol* 184: 830–838, 2003.
- Hodgkin AL, Huxley AF. A quantitative description of membrane current and its application to conduction and excitation in nerve. *J Physiol* 117: 500–544, 1952.
- Hossain WA, Antic SD, Yang Y, Rasband MN, Morest DK. Where is the spike generator of the cochlear nerve? Voltage-gated sodium channels in the mouse cochlea. *J Neurosci* 25: 6857–68, 2005.
- Khalil ZM, Gouwens NW, Raman IM. The contribution of resurgent sodium current to high-frequency firing in Purkinje neurons: an experimental and modeling study. *J Neurosci* 23: 4899–4912, 2003.
- Khalil ZM, Raman IM. Relative contributions of axonal and somatic Na channels to action potential initiation in cerebellar Purkinje neurons. *J Neurosci* 26: 1935–1944, 2006.
- Klöckner U, Lee JH, Cribbs LL, Daud A, Hescheler J, Pereverzev A, Perez-Reyes E, Schneider T. Comparison of the Ca²⁺ currents induced by expression of three cloned α_1 subunits, α_{1G} , α_{1H} and α_{1I} , of low-voltage-activated T-type Ca²⁺ channels. *Eur J Neurosci* 11: 4171–4178, 1999.
- Kohrman DC, Harris JB, Meisler MH. Mutation detection in the med and medl alleles of the sodium channel *Scn8a*. Unusual splicing due to a minor class AT-AC intron. *J Biol Chem* 271: 17576–81, 1996.
- Kole MH, Ilschner SU, Kampa BM, Williams SR, Ruben PC, Stuart GJ. Action potential generation requires a high sodium channel density in the axon initial segment. *Nat Neurosci* 11: 178–186, 2008.
- Lee JH, Daud AN, Cribbs LL, Lacerda AE, Pereverzev A, Klockner U, Schneider T, Perez-Reyes E. Cloning and expression of a novel member of the low voltage-activated T-type calcium channel family. *J Neurosci* 19: 1912–1921, 1999.
- Levin SI, Khalil ZM, Aman TK, Grieco TM, Kearney JA, Raman IM, Meisler MH. Impaired motor function in mice with cell-specific knockout of sodium channel *Scn8a* (Nav1.6) in cerebellar purkinje neurons and granule cells. *J Neurophysiol* 96: 785–793, 2006.
- Magistretti J, Alonso A. Biophysical properties and slow voltage-dependent inactivation of a sustained sodium current in entorhinal cortex layer-II principal neurons: a whole-cell and single-channel study. *J Gen Physiol* 114: 491–509, 1999.
- Martin MS, Tang B, Papale LA, Yu FH, Catterall WA, Escayg A. The voltage-gated sodium channel *Scn8a* is a genetic modifier of severe myoclonic epilepsy of infancy. *Hum Mol Genet* 16: 2892–2899, 2007.
- Maurice N, Tkatch T, Meisler M, Sprunger LK, Surmeier DJ. D1/D5 dopamine receptor activation differentially modulates rapidly inactivating and persistent sodium currents in prefrontal cortex pyramidal neurons. *J Neurosci* 21: 2268–2277, 2001.
- McAllister-Williams RH, Kelly JS. The temperature dependence of high-threshold calcium channel currents recorded from adult rat dorsal raphe neurons. *Neuropharmacology* 34: 1479–1490, 1995.

- McCormick DA, Shu Y, Yu Y.** Neurophysiology: Hodgkin and Huxley model—still standing? *Nature* 445: E1–E2, 2007.
- Meeks JP, Mennerick S.** Action potential initiation and propagation in CA3 pyramidal axons. *J Neurophysiol* 97: 3460–3472, 2007.
- Mercer JN, Chan CS, Tkatch T, Held J, Surmeier DJ.** Nav1.6 sodium channels are critical to pacemaking and fast spiking in globus pallidus neurons. *J Neurosci* 27: 13552–13566, 2007.
- Migliore M, Hoffman DA, Magee JC, Johnston D.** Role of an A-type K^+ conductance in the back-propagation of action potentials in the dendrites of hippocampal pyramidal neurons. *J Comput Neurosci* 7: 5–15, 1999.
- Naundorf B, Wolf F, Volgushev M.** Unique features of action potential initiation in cortical neurons. *Nature* 440: 1060–1063, 2006.
- Noda M, Ikeda T, Suzuki H, Takeshima H, Takahashi T, Kuno M, Numa S.** Expression of functional sodium channels from cloned cDNA. *Nature* 322: 826–828, 1986.
- Ogiwara I, Miyamoto H, Morita N, Atapour N, Mazaki E, Inoue I, Takeuchi T, Itohara S, Yanagawa Y, Obata K, Furuichi T, Hensch TK, Yamakawa K.** Na(v)1.1 localizes to axons of parvalbumin-positive inhibitory interneurons: a circuit basis for epileptic seizures in mice carrying an scn1a gene mutation. *J Neurosci* 27: 5903–5914, 2007.
- Palmer LM, Stuart GJ.** Site of action potential initiation in layer 5 pyramidal neurons. *J Neurosci* 26: 1854–1863, 2006.
- Pan Z, Kao T, Horvath Z, Lemos J, Sul JY, Cranstoun SD, Bennett V, Scherer SS, Cooper EC.** A common ankyrin-G-based mechanism retains KCNQ and NaV channels at electrically active domains of the axon. *J Neurosci* 26: 2599–2613, 2006.
- Raman IM, Bean BP.** Resurgent sodium current and action potential formation in dissociated cerebellar Purkinje neurons. *J Neurosci* 17: 4517–4526, 1997.
- Raman IM, Sprunger LK, Meisler MH, Bean BP.** Altered subthreshold sodium currents and disrupted firing patterns in Purkinje neurons of Scn8a mutant mice. *Neuron* 19: 881–891, 1997.
- Randall AD, Tsien RW.** Contrasting biophysical and pharmacological properties of T-type and R-type calcium channels. *Neuropharmacology* 36: 879–893, 1997.
- Rush AM, Dib-Hajj SD, Waxman SG.** Electrophysiological properties of two axonal sodium channels, Nav1.2 and Nav1.6, expressed in mouse spinal sensory neurones. *J Physiol* 564: 803–815, 2005.
- Shirahata E, Iwasaki H, Takagi M, Lin C, Bennett V, Okamura Y, Hayasaka K.** Ankyrin-G regulates inactivation gating of the neuronal sodium channel, Nav1.6. *J Neurophysiol* 96: 1347–1357, 2006.
- Shu Y, Duque A, Yu Y, Haider B, McCormick DA.** Properties of action-potential initiation in neocortical pyramidal cells: evidence from whole cell axon recordings. *J Neurophysiol* 97: 746–760, 2007.
- Smith MR, Smith RD, Plummer NW, Meisler MH, Goldin AL.** Functional analysis of the mouse Scn8a sodium channel. *J Neurosci* 18: 6093–6102, 1998.
- Sochivko D, Chen J, Becker A, Beck H.** Blocker-resistant Ca^{2+} currents in rat CA1 hippocampal pyramidal neurons. *Neuroscience* 116: 629–638, 2003.
- Sochivko D, Pereverzev A, Smyth N, Gissel C, Schneider T, Beck H.** The Cav2.3 calcium channel subunit contributes to R-type calcium currents in murine hippocampal and neocortical neurones. *J Physiol* 542.3: 600–710, 2002.
- Stacey WC, Durand DM.** Stochastic resonance improves signal detection in hippocampal CA1 neurons. *J Neurophysiol* 83: 1394–1402, 2000.
- Stuart G, Hausser M.** Initiation and spread of sodium action potentials in cerebellar Purkinje cells. *Neuron* 13: 703–712, 1994.
- Stuart G, Schiller J, Sakmann B.** Action potential initiation and propagation in rat neocortical pyramidal neurons. *J Physiol* 505: 617–632, 1997a.
- Stuart GJ, Sakmann B.** Active propagation of somatic action potentials into neocortical pyramidal cell dendrites. *Nature* 367: 69–72, 1994.
- Su H, Sochivko D, Becker A, Chen J, Jiang Y, Yaari Y, Beck H.** Upregulation of a T-Type Ca^{2+} channel causes a long-lasting modification of neuronal firing mode after status epilepticus. *J Neurosci* 22: 3645–3655, 2002.
- Swensen AM, Bean BP.** Robustness of burst firing in dissociated purkinje neurons with acute or long-term reductions in sodium conductance. *J Neurosci* 25: 3509–3520, 2005.
- Takahashi K, Akaike N.** Calcium antagonist effects on low-threshold (T-type) calcium current in rat isolated hippocampal CA1 pyramidal neurons. *J Pharmacol Exp Ther* 256: 169–175, 1991.
- Van Wart A, Matthews G.** Impaired firing and cell-specific compensation in neurons lacking nav1.6 sodium channels. *J Neurosci* 26: 7172–7180, 2006.
- Van Wart A, Trimmer JS, Matthews G.** Polarized distribution of ion channels within microdomains of the axon initial segment. *J Comp Neurol* 500: 339–352, 2007.
- Varona P, Ibarz JM, Lopez-Aguado L, Herreras O.** Macroscopic and subcellular factors shaping population spikes. *J Neurophysiol* 83: 2192–2208, 2000.
- Warman EN, Durand DM, Yuen GLF.** Reconstruction of hippocampal CA1 pyramidal cell electrophysiology by computer simulation. *Neurophysiology* 2033–2045, 1994.
- Yue C, Remy S, Su H, Beck H, Yaari Y.** Proximal persistent Na^+ channels drive spike afterdepolarizations and associated bursting in adult CA1 pyramidal cells. *J Neurosci* 25: 9704–9720, 2005.
- Zhou D, Lambert S, Malen PL, Carpenter S, Boland LM, Bennett V.** AnkyrinG is required for clustering of voltage-gated Na channels at axon initial segments and for normal action potential firing. *J Cell Biol* 143: 1295–1304, 1998.